ISSN (Print) 1226-1750
ISSN (Online) 2233-6656
Journal of Magnetics 31(3), 290-313 (2026) https://doi.org/10.4283/JMAG.2026.31.3.290

Comparative Study of Performance between Permanent-Magnet-Excited Homopolar Inductor Alternator and PMSM for High-Speed Drive Systems

Long-jian Liu[1], Ke-xun Yu[2], Xian-fei Xie[2], and Zhi-jian Liu[1]*

[1]*Faculty of Electric Power Engineering, Kunming University of Science and Technology, Kunming 650500, China*
[2]*State Key Laboratory of Advanced Electromagnetic Technology, School of Electrical and Electronic Engineering, Huazhong University of Science and Technology, Wuhan 430074, China*

(Received 24 January 2025, Received in final form 7 September 2026, Accepted 9 September 2026)

To guide the selection between permanent-magnet-excited (PME) homopolar inductor alternators (HIAs) and permanent magnet synchronous machines (PMSMs), the performance of a 1 MW PME HIA and PMSM operating at a rotational speed of 22,000 r/min is compared. The study demonstrates that, depending on the relative magnitudes of the *d*-axis and *q*-axis synchronous inductances, the PME HIA can be equivalently represented as a salient-pole, surface-mounted, or interior PMSM with radially magnetized permanent magnets. The equivalent permanent magnets exhibit significantly higher coercive force and substantially reduced thickness compared with conventional PMSM designs. Furthermore, the optimal rotor pole embrace design is identical to that of the radial-magnetized PMSM. The fundamental component of the air-gap magnetic flux density and the power density of the PME HIA are comparable to those of the PMSM. However, the 3rd harmonic of the no-load air-gap magnetic field and induced phase voltage for the PME HIA are significantly larger than those of the parallel-magnetized PMSM, whereas the line-to-line induced voltage harmonics are comparable. The synchronous inductance of the PME HIA is substantially larger than that of the PMSM due to a considerably smaller equivalent air-gap length, while its leakage inductance is significantly smaller owing to the slotless stator-core structure. Moreover, the PME HIA with an air-gap winding exhibits 2% higher efficiency and significantly superior reliability compared with the PMSM. The temperature rise of the PME HIA is substantially lower than that of the PMSM, primarily due to significantly reduced winding copper losses in the effective parts. The construction of a prototype machine is planned, and experimental tests will be conducted to validate the analytical results presented in this paper. This study provides valuable guidance for machine selection and enhances the understanding of comparisons between PME HIAs and PMSMs.

Keywords : permanent magnet excited HIA, air-gap winding, high-speed driving systems, PMSM

1. Introduction

Permanent magnet synchronous machines (PMSMs) offer the advantages of high-power density and efficiency [1–3]. However, due to their complex rotor structures, their reliability is limited, particularly in high-speed drive systems. Furthermore, the rotor magnets in PMSMs are susceptible to demagnetization caused by high temperatures resulting from eddy-current losses. Numerous studies have addressed the design [4,5], thermal modeling [6,7], and performance validation [8] of high-speed PMSMs. The severe squeezing effects on the armature winding in high-speed PMSMs pose significant thermal challenges. To mitigate this issue, air-gap windings [9,10] and Litz wire [4,5] can be employed. Studies [11,12] have shown that slotless motors achieve higher torque than slotted motors when thermal constraints are not considered; however, under thermal limitations, slotted motors can deliver higher maximum torque.

The homopolar inductor alternator (HIA) has gained popularity in various applications owing to its high-power density and reliability, which are primarily attributed to its simple rotor structure. HIAs have been successfully deployed in diverse fields, including pulsed power supplies [13–18], flywheel energy storage [19–24], airborne applications [25], and ship propulsion systems [26].

In permanent-magnet-excited (PME) HIAs, the eddy-current losses in the permanent magnets are minimal, and

©The Korean Magnetics Society. All rights reserved.
*Corresponding author: +86-871-65916839
E-mail: liuzhijian_kust@163.com, liuzhijian@kust.edu.cn

the heat dissipation conditions are significantly superior to those in PMSMs. Consequently, the temperature rise is extremely low, and there is no risk of magnet demagnetization. In high-speed HIAs with slotted stator cores, the squeezing effects on the winding represent a significant concern [16], which can adversely affect machine performance. Moreover, compared with PMSMs, the fundamental air-gap magnetic flux density in HIAs with slotted stator cores is lower. To address these issues, similar to the method of slotless PMSM [9-12], a PME HIA with an air-gap winding was proposed in our previous study [27]. The optimal design for minimum mass and the relationships among air-gap magnetic flux density, unit number, shell diameter, and mass were investigated in [27]. The results demonstrated that this novel approach effectively reduces armature winding copper losses compared with conventional PME HIAs.

The flowchart of this paper is shown in Fig. 1. The key performance parameters for machines used in high-speed drive systems include power density, EMF harmonic distortion, winding inductance, efficiency, temperature rise, and reliability. Power density is critical for overall mass; efficiency and temperature rise significantly affect machine lifetime; and reliability is essential for defense applications. EMF harmonic distortion substantially influences torque ripple, which affects operational stability and can cause significant vibration and noise. Inductance plays a major role in dynamic performance characteristics such as commutation and torque ripple, as well as steady-state performance such as average torque. An appropriate inductance is necessary to achieve excellent dynamic and steady-state performance. The objective of this paper is to determine which machine type—PME HIA or PMSM—is more suitable for high-speed drive applications.

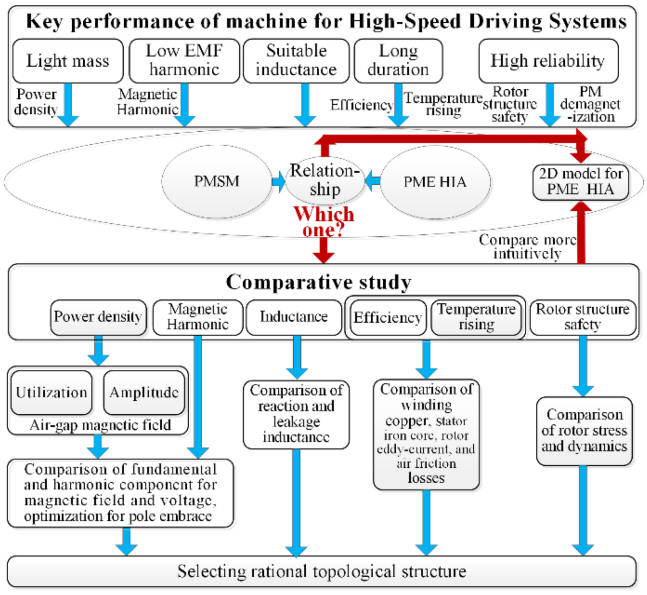


Fig. 1. (Color online) The flow chart of this paper.

Regarding power density, it is well established that the power density of an electrical machine is proportional to the fundamental component of the air-gap magnetic field. Generally, PME HIAs are considered to have lower power density than PMSMs because the air-gap magnetic field utilization in PME HIAs is substantially lower than that in PMSMs. However, for PME HIAs with air-gap windings, the air-gap magnetic flux density is higher than that in PMSMs, making it difficult to determine which machine achieves higher power density. Regarding efficiency, the armature winding copper losses in PME HIAs are lower than those in PMSMs, but the rotor eddy-current losses are higher. Therefore, it is also difficult to determine which machine offers higher efficiency. Regarding inductance, no studies have compared the inductances of PME HIAs and PMSMs. Regarding temperature rise, the armature winding temperature rise in PME HIAs is lower than that in PMSMs; however, the high rotor eddy-current losses in PME HIAs may cause serious overheating issues in the rotor, making it difficult to determine which machine exhibits lower temperature rise. Regarding EMF harmonic distortion, it is generally accepted that the magnetic field harmonics and phase EMF harmonics in HIAs are significantly higher than those in PMSMs, but the situation for line-to-line EMF remains unclear. Furthermore, no studies have investigated whether the optimization of pole embrace to reduce EMF harmonics in PME HIAs follows the same approach as in PMSMs.

To guide the selection between PME HIAs and PMSMs, these performance characteristics must be carefully compared. To facilitate an intuitive comparison between PME HIAs and PMSMs, the relationship between these two machine types must first be investigated. However, no studies have addressed the performance comparison between PME HIAs and PMSMs or the relationship between these machines. Moreover, whether the optimization of pole embrace in PME HIAs to maximize the fundamental component of the air-gap magnetic field while simultaneously minimizing the 5th harmonic of the air-gap magnetic field follows the same approach as in PMSMs remains uninvestigated.

To guide the selection between PME HIAs and PMSMs, this paper presents a comprehensive comparative study of the performance of PME HIAs and PMSMs for high-speed drive systems.

The structure of this paper is organized as follows. First, an equivalent 2D model for the PME HIA is introduced to facilitate intuitive comparison with the PMSM.

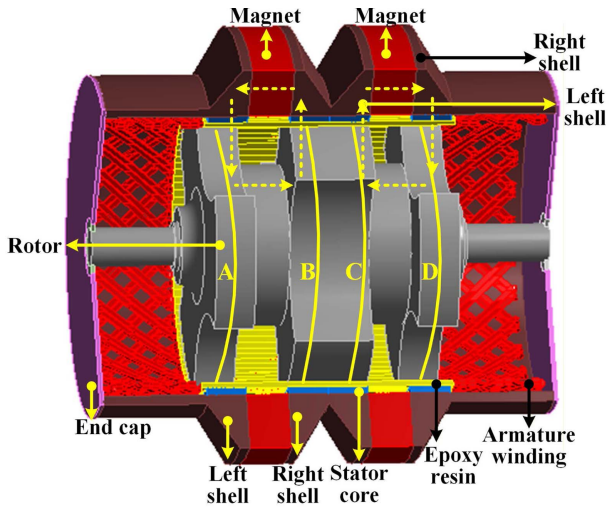
Next, the optimization of pole embrace for the PME HIA is investigated using the 2D model and compared with that of the PMSM. Subsequently, the design considerations and results for a 1 MW PME HIA and PMSM operating at 22,000 r/min are briefly presented. For comparison purposes, the RMS values of the no-load induced voltages are designed to be identical for both machines. Finally, a detailed comparison between the PME HIA and PMSM is presented, focusing on no-load air-gap magnetic field, no-load induced voltage harmonics, power density, inductance, losses and efficiency, temperature rise, rotor structural safety, and reliability. For power density and inductance, theoretical analytical analyses are conducted first, followed by FEM simulations to validate the analytical results.

The results demonstrate that the PME HIA offers superior performance in terms of losses, efficiency, temperature rise, and reliability. Furthermore, the fundamental component of the air-gap magnetic flux density in the HIA is comparable to that in PMSMs, and the power density is only 2% lower than that of the PMSM. The reaction inductance of the PME HIA is significantly higher than that of the PMSM, whereas the leakage inductance is substantially lower. This study provides valuable guidance for machine selection and enhances understanding of the comparisons between PME HIAs and PMSMs.

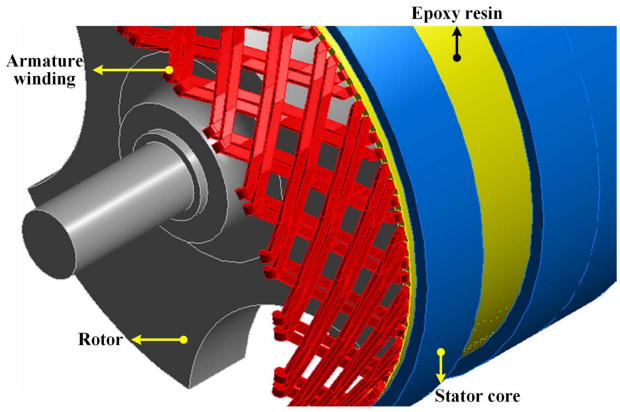
2. Equivalent 2D model of PME HIA

The structure of a conventional PME HIA is illustrated in Fig. 2(a). The permanent magnet is positioned between the left and right shells, and an air-gap winding is employed. The structure supporting the winding is depicted in Fig. 2(b).

As demonstrated in [28], the electrically excited (EE) HIA can be modeled as a wound-field synchronous machine and represented using an equivalent 2D model [29]. Similarly, the PME HIA can also be represented by an equivalent 2D model, as shown in Fig. 3. In this model, HIA Part 1 comprises a rotor formed by the overlap of the left and right rotors, while HIA Part 2 consists of a smooth rotor with a diameter equal to that of the rotor shaft. The combination of HIA Parts 1 and 2 equivalently represents the magnetically active portion of the HIA, which comprises left and right sections. The axial lengths of both HIA Parts 1 and 2 are equal to the length of either the left or right half of the rotor. The armature windings of HIA Parts 1 and 2 are connected in series, and the end-winding inductance is represented by an external inductance connected in series with the two



(a) PME HIA



(b) The structure supporting air-gap winding

Fig. 2. (Color online) The structures of multi-unit PME HIA and the air-gap winding.

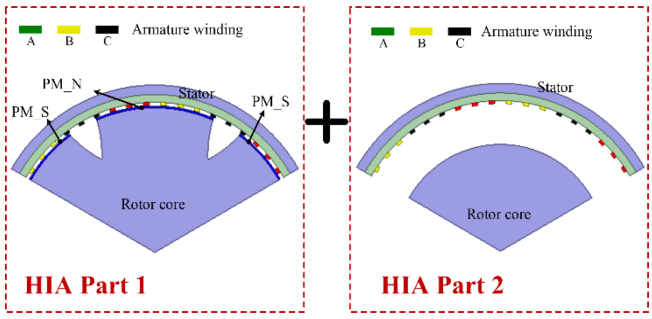


Fig. 3. (Color online) The equivalent 2D model of PME HIA.

parts. It can be observed that the field coil in the 2D model of the EE HIA is replaced by a permanent magnet, with the arc length of the magnet equal to the rotor tooth width. Since the ratio of rotor slot width to tooth pitch is selected to be approximately 0.6, the N-pole and S-pole magnets do not intersect. Consequently, the PME HIA

can be regarded as equivalent to a PMSM. The rotor core in the 2D model is a salient-pole rotor, rather than the smooth rotor core used in PMSMs.

When the effects of axial magnetomotive force drop on the winding inductance are neglected, the above equivalent method ensures that the armature winding inductance of the equivalent 2D model matches that of the actual 3D PME HIA model. The discussion of cases where the axial magnetomotive force drop is considered will be presented subsequently.

Next, the coercive force of the permanent magnet in the equivalent 2D model must be determined. The amplitude of the no-load air-gap magnetic field should be identical for both the equivalent 2D model and the actual 3D model of the PME HIA. Based on this requirement, the coercive force of the permanent magnet in the equivalent 2D model can be calculated as follows.

According to the magnetic equivalent circuit model shown in Fig. 4, the magnetomotive force of the equivalent permanent magnet in the 2D model for the PME HIA is:

$$F_\delta = F_{pm}\frac{R_\delta R_{ms}}{2R_\delta + R_{ms}} \Bigg/ \left(\frac{2R_\delta R_{ms}}{2R_\delta + R_{ms}} + R_m\right) \tag{1}$$

Where, the F_{pm}, R_δ, R_{ms}, and R_m are defined in Appendix. Assuming the thickness of PM in the 2D model is h_{me}, then the equivalent coercive force H_{ce} can be obtained that, to be:

$$H_{ce} = \frac{F_\delta}{h_{me}} \tag{2}$$

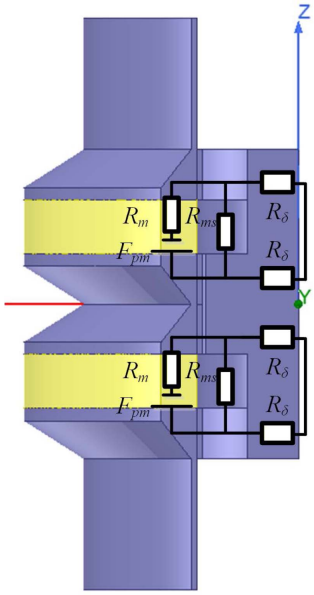


Fig. 4. (Color online) Magnetic equivalent circuit model for PME HIA.

When ignoring the effect of R_{ms}, then it can be obtained that:

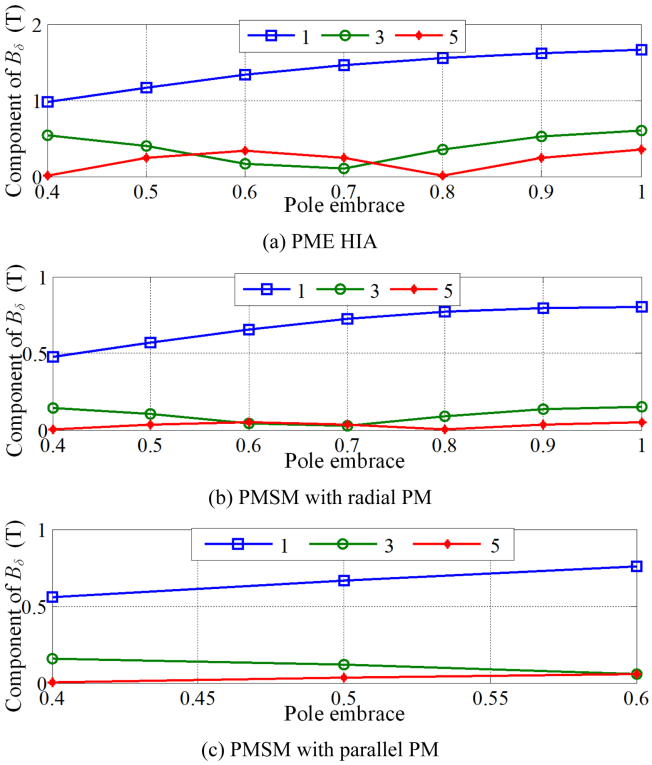
$$H_{ce} = \frac{l_m B_m}{\mu_0 \mu_r h_{me}} \frac{R_\delta}{2R_\delta + R_m} \tag{3}$$

It can be seen that, when the l_m is much larger than the h_{me}, for the PME HIA, in the 2D model, the equivalent H_{ce} in the 2D model is much larger than the PMSM.

3. Comparisons of optimization for pole embrace using 2D model

3.1. Harmonic of no-load air-gap magnetic field

From the 2D model of the PME HIA, it can be derived that varying the permanent magnet width results in different waveforms of the no-load air-gap magnetic field. The relationship between the harmonic components of the no-load air-gap magnetic field and the pole embrace, as obtained from the 2D model, is presented in Fig. 5(a). Since the air-gap reluctance is significantly smaller than that of the permanent magnet and remains relatively constant with varying pole embrace, the magnet thickness in the 2D model is assumed to be constant for simplified analysis. The relationship between the HIA rotor tooth



(a) PME HIA

(b) PMSM with radial PM

(c) PMSM with parallel PM

Fig. 5. (Color online) The relationship between the harmonic components of no-load air-gap magnetic field and the pole embrace.

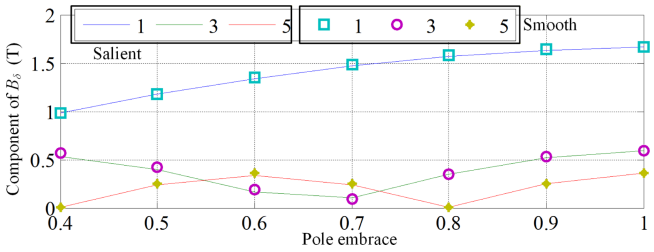


Fig. 6. (Color online) The comparison of air-gap magnetic field for equivalent 2D model with smooth rotor or salient-pole rotor.

width coefficient k_w and the pole embrace α_p is expressed as:

$$\alpha_p = 2k_w \tag{4}$$

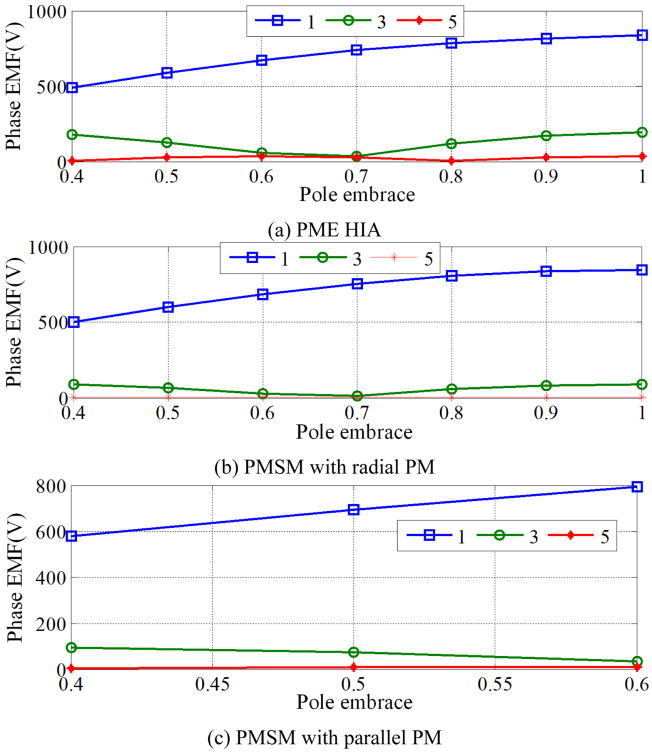
Here, the rotor tooth width coefficient k_w for the HIA is defined as the ratio of the rotor tooth width to the rotor tooth pitch. For comparison, the results for PMSMs with radial and parallel magnetization are also presented in Figs. 5(b) and 5(c), respectively. It can be observed that the variation trends are identical for the PME HIA and the radial-magnetized PMSM. To minimize the 3rd harmonic of the air-gap magnetic field, parallel magnetization can be adopted. However, since the winding is Y-connected, the 3rd harmonic can be neglected because it does not contribute to the line-to-line voltage.

For the PME HIA, the pole embrace is selected to be approximately 0.8, as this value yields a large fundamental component while minimizing the 5th harmonic. Similarly, for the radial-magnetized PMSM, the pole embrace is also chosen to be approximately 0.8 for the same reasons. In contrast, for the parallel-magnetized PMSM, the optimal pole embrace is 0.6. Consequently, the PME HIA can be regarded as equivalent to a radial-magnetized PMSM, and the optimal rotor pole embrace design follows the same principle as that for radial-magnetized PMSMs.

Fig. 6 presents a comparison between equivalent 2D models with smooth and salient-pole rotors. It can be seen that, for simplified analysis of the air-gap magnetic field, the HIA rotor can be approximated as a smooth rotor in the equivalent 2D model.

3.2. Harmonic of no-load induced voltage

For the PME HIA, the relationship between the harmonic components of the no-load induced phase voltage and the pole embrace, as obtained from the 2D model, is presented in Fig. 7(a). For comparison, the results for PMSMs with radial and parallel magnetization are also shown in Figs. 7(b) and 7(c), respectively. It can be observed that the

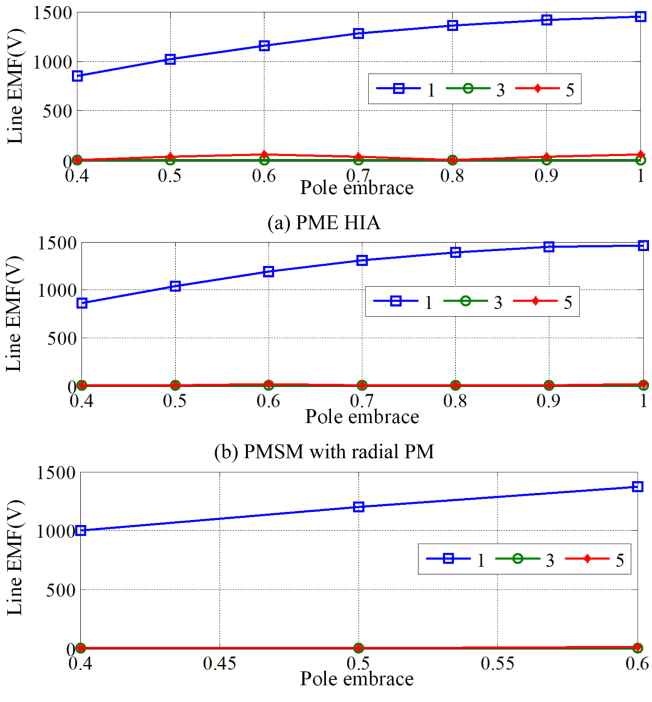


(a) PME HIA

(b) PMSM with radial PM

(c) PMSM with parallel PM

Fig. 7. (Color online) The relationship between the harmonic components of no-load phase induced voltage and the pole embrace.



(a) PME HIA

(b) PMSM with radial PM

(c) PMSM with parallel PM

Fig. 8. (Color online) The relationship between the harmonic components of no-load line-to-line induced voltage and the pole embrace.

variation trends of the induced phase voltage closely follow those of the magnetic field. However, the 5th harmonic of the phase voltage is significantly attenuated due to the distributed winding configuration. Regarding the 3rd harmonic of the phase voltage, the PME HIA and the radial-magnetized PMSM exhibit comparable levels, whereas the parallel-magnetized PMSM shows a much smaller 3rd harmonic component.

The results for the line-to-line induced voltage are presented in Fig. 8. It can be seen that all harmonic components are small for the PME HIA and for both the radial- and parallel-magnetized PMSMs. This is because the 3rd harmonic is eliminated in the line-to-line voltage due to the Y-connected winding configuration.

4. Design Considerations

4.1. The input parameters for designing

The input parameters for designing the PME HIA and PMSM are displayed in Table 1.

4.2. Design considerations for HIA

The design considerations for the HIA are as follows:

(1) Pole-pair number selection: Considering both the reduction of electrical frequency and overall weight, the pole-pair number is selected as 3. The electrical frequency is primarily constrained by the IGBT switching frequency of the motor controller.

(2) Rotor slot depth: The rotor slot depth is chosen to be approximately 11 times the air-gap length. Under this condition, the fundamental component of the air-gap magnetic field can achieve a reasonable level, while the rotor slot depth is not excessively large to avoid significantly compromising rotor mechanical strength.

(3) Rotor slot width-to-tooth-pitch ratio: In the analytical design of the PME HIA, the ratio of rotor slot width to tooth pitch is selected as approximately 0.6, rather than 0.55 as reported in our previous conference paper [27]. This modification aims to maximize the fundamental component of the air-gap magnetic field while simultaneously minimizing the 5th harmonic. The reason for selecting 0.6 instead of 0.55 is that the reduction of the 5th harmonic was not considered in the conference paper [27].

(4) Maximum air-gap magnetic flux density: The maximum air-gap magnetic flux density is approximately 1.5 T, which is determined by the saturation flux density of the rotor material.

The calculation results presented in [27] demonstrate that the air-gap magnetic flux density B_δ, the unit number of the HIA K_{mu}, and the shell diameter D_{shell} significantly impact the overall mass. Therefore, these parameters were selected for optimization. As shown in Table 2, the variation ranges are as follows: from 1.0 T to 1.5 T, with options of 1, 2, and 3, and from 0.43 m to 0.53 m.

Table 2. The optimization parameters of PME HIA [27].

Parameters	Variation
Maximum magnetic flux density of the air gap B_δ	1.0-1.5 T
Unit number of stator core K_{mu}	1-3
Maximum outer diameter of shell D_{shell}	0.43-0.53 m

Table 1. The input parameters for designing the PME HIA and PMSM and the same constraints when comparing two machines [27].

Parameters	Value
Input parameter	
Maximum value of rotating speed (r/min)	22000
Maximum value of electrical frequency (Hz)	≤ 1100
Maximum value of output power (MW)	1
Total weight of motor (kg)	≤250
Rated efficiency	≥96%
Continuous operating time (s)	≥100, only one cycle
The same constraints	
Geometric envelope	Outer diameter<0.53 m
Thermal class insulation	Both are C class
Electrical constraints	Identical DC bus voltage, current, and switching frequency
Operating point	Both @ 22000 r/min and 1 MW
Control mode	Both are square wave
Cooling condition	Both are water cooling at the casing

Table 3. The optimization results of the PME HIA.

Parameters	Non-optimization	Optimization for M_t	Optimization for M_{PM}	Optimization for M_W
Maximum value of air-gap magnetic flux density B_δ (T)	1.0	1.5	1.0	1.5
Unit number of stator core K_{mu}	1	2	1	2
Maximum outer diameter of shell D_{shell} (m)	0.43	0.43	0.51	0.45
Mass of machine M_t (kg)	342	239	317	240
Mass of permanent magnet M_{PM} (kg)	62	51	21	46
Weighted mass M_W (kg)	286	201.4	257.8	201.2

In this paper, a weighted objective function incorporating mass considerations is employed. The weighted mass objective function is defined as:

$$M_W = K_t M_t + K_{PM} M_{PM} \tag{5}$$

where M_W represents the weighted mass, M_t denotes the total mass, and M_{PM} indicates the permanent magnet mass. The values of M_t and M_{PM} are determined by B_δ, D_{shell} and K_{mu}; their calculation formulas can be found in [27]. The weighting coefficients K_t and K_{PM} represent the weights assigned to the total mass and permanent magnet mass, respectively.

It is important to emphasize that the total machine mass significantly affects performance, whereas the permanent magnet mass has a relatively minor impact. The total mass plays a vital role in defense applications, while the magnet mass primarily influences cost, which is considered less critical. Consequently, the weighting coefficient for total mass, M_t, is substantially larger than that for the permanent magnet mass, K_{PM}. Here, K_t and K_{PM} are selected as 0.8 and 0.2, respectively.

Table 3 presents the values of B_δ, D_{shell}, and K_{mu} for non-optimized cases, as well as the optimal values M_t, M_{PM}, and M_W. It can be observed that optimizing M_{PM} reduces the permanent magnet mass from 62 kg to 21 kg. Similarly, optimizing M_t decreases the total machine mass from 342 kg to 239 kg. By optimizing M_W, the optimal values of K_{mu}, B_δ, and D_{shell} are obtained as 2, 1.5 T, and 0.45 m, respectively (as shown in Table 3). In this case, the total mass of the PME HIA approaches its minimum value while the permanent magnet mass remains within acceptable limits.

4.3. Design considerations for PMSM

To ensure a fair comparison between the PME HIA and the PMSM, the PMSM is designed with identical rotational speed, pole-pair number, stator slot number, and winding pitch. Additionally, the cooling for both machines is maintained at the same level. The main design considerations for the PMSM are outlined below.

(1) Rotor configuration: A surface-mounted permanent magnet rotor is selected for high-speed applications due to its superior reliability compared with interior permanent magnet rotors. The magnets are bonded to the rotor core using a retaining sleeve.

(2) Sleeve material selection: Carbon fiber T300 is chosen as the sleeve material because metallic sleeves exhibit excessively high eddy-current losses—simulation results indicate that such losses could reach several tens of kilowatts.

(3) Stator core structure: The PMSM stator core employs a slotted structure, as it is impractical to install armature windings directly in the air gap. Semi-closed slots are preferred over open slots to minimize rotor eddy-current losses induced by tooth harmonic magnetic fields.

(4) Winding configurations: To facilitate comparison with the PME HIA, two winding designs are considered: Litz wire and conventional non-Litz wire.

(5) Sleeve design parameters: The sleeve thickness and interference fit are determined using the methods presented in [30], with FEM simulations employed to optimize the interference value.

Through these design considerations, the PMSM can be effectively evaluated against the PME HIA in terms of overall performance. This study aims to provide valuable insights for future developments in this field.

5. Designed Results

Table 4 presents the designed parameters of the PME HIA, while those of the PMSM are given in Table 5. The materials employed for both machines are summarized in Table 6. It should be noted that the PMSM winding incorporates three parallel branches, whereas the PME HIA has only one. Additionally, the number of conductors per slot is two for the PMSM and one for the PME HIA.

A comparison between the 3D models of the PMSM and the PME HIA, shown in Fig. 9 and Fig. 2, respec-

Table 4. Designed parameters of PME HIA [27].

Symbol	Parameter	Value
D	Rotor diameter (mm)	304
p	Pole pair number	3
h	Rotor groove depth (mm)	68
l	Stator core length (mm)	41
l_b	Shaft length (mm)	44
δ	Air-gap length (mm)	6
D_i	Inner diameter of stator core (mm)	316
D_o	Outer diameter of stator core (mm)	332
z_1	Stator slots	54
l_m	Length of permanent magnet (mm)	44
D_{shell}	Outer diameter of the shell (mm)	450
D_{shaft}	Rotor shaft diameter (mm)	168
a	Number of parallel branches	1
q	Number of slots per pole per phase	3
N_l	Winding layers	1
n_c	Number of conductors per slot	1
N	Number of series turns per phase	9
k_N	Winding coefficient	0.96
β	Short pitch coefficient of armature winding	1
B_δ	Maximum magnetic flux density of the air gap (T)	1.5
n_r	Rotating speed (r/min)	5500 or 22000
K_{mu}	Unit number of HIA	2
J_c	Current density (A/mm^2)	Flat wire: 12 Litz wire: 13
n_{cs}	Number of sub-conductors	Flat wire: 13 Litz wire: 1
S_{cs}	Area of sub-conductors (mm^2)	Flat wire: 4 Litz wire: 16
w_{cs}	Width of sub-conductors (mm)	Flat wire: 4 Litz wire: 4
h_{cs}	Thickness of sub-conductors (mm)	Flat wire: 1 Litz wire: 4.8
η_s	Slot fill factor	Flat wire: 48% Litz wire: 42%

tively, reveals a significant difference in axial length. This disparity stems from the substantially higher permissible rotor tip speed of the PME HIA, whereas the complex rotor structure of the PMSM constrains the rotor tip speed, necessitating a relatively smaller rotor diameter.

6. Comparisons of no-load air-gap magnetic field and induced voltage

6.1. The no-load air-gap magnetic field

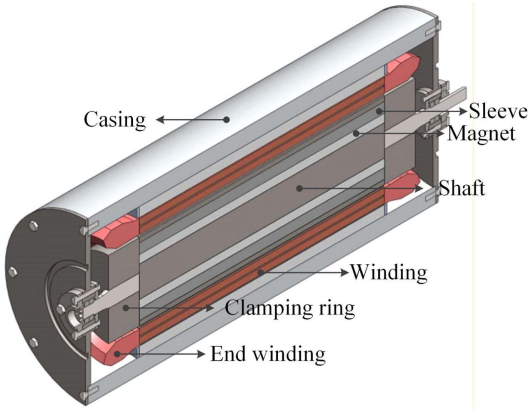
To validate the results obtained from the equivalent 2D model, case studies were conducted using the machines with parameters given in Tables 4 and 5. The relationships between the harmonic components of the no-load air-gap magnetic field and the pole embrace for the PME HIA, as well as those of the no-load phase induced voltage, are presented in Figs. 10(a) and 10(b), respectively, based on 3D FEM simulations. The magnetic flux density of the PME HIA is determined as the sum of the left and right components. To account for axial variations, the results at different axial positions (A, B, C, and D) in the air gap, as shown in Fig. 2(a), were averaged. It can be observed that the results are generally consistent with those of the equivalent 2D model.

Table 5. Designed parameters of PMSM.

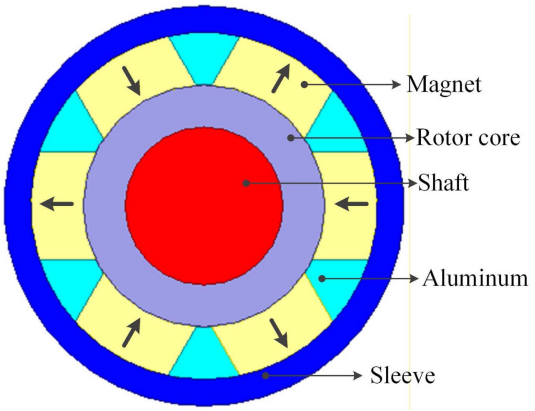
Symbol	Parameter	Value
D_{ro}	Outer diameter of rotor (mm)	132
p	Number of pole pair	3
h_M	Thickness of magnet (mm)	20
n_{Ms}	Number of slices for magnet in axial direction	20
l	Length of rotor or stator (mm)	570
D_{ri}	Inner diameter of rotor (mm)	60
δ	Air-gap length (mm)	10
D_i	Inner diameter of stator-core (mm)	152
D_o	Outer diameter of stator-core (mm)	255
z_1	Stator slots	54
z_{sk}	Skew width in slot number	1
α_p	Mechanical pole embrace	0.6
D_{shell}	Outer diameter of casing (mm)	315
a	Number of parallel branches	3
q	Stator slot number per pole per phase	3
N_l	Winding layers	2
n_c	Number of conductors per slot	2
N	Number of series turn number per phase	6
β	Short pitch coefficient of armature winding	1
B_δ	Maximum magnetic flux density of air gap (T)	0.7
n_r	Rotating speed (r/min)	5500 or 22000
J_c	Current density (A/mm^2)	Enameled round wire: 5.2 Litz wire: 12
b_{s0}	Slot opening width (mm)	2
h_{s0}	Slot opening height (mm)	1
h_{s1}	Slot wedge height (mm)	1
b_{s1}	Slot wedge maximum width (mm)	4
h_{s2}	Slot body height (mm)	27.5
b_{s2}	Slot body bottom width (mm)	6.9
r_{ss}	Slot body bottom fillet (mm)	4
η_s	Slot fill factor	Enameled round wire: 60% Litz wire: 25%

Table 6. Materials of PME HIA and PMSM.

Component	PME HIA	Component	PMSM
Stator iron core	Silicon steel sheet (DW-310-35)	Stator iron core	DW-310-35
Casing	Carbon steel (Q235)	Casing	Aluminum alloy
Rotor core	Alloy steel (40CrNiMoA)	Rotor core	DW-310-35
PM	NdFeB N42UH	PM	N42UH
Armature winding	Copper	Armature winding	Copper
Rotor shaft	40CrNiMoA	Rotor shaft	Q235
Winding supporting structure	Epoxy resin	Rotor sleeve	Carbon fiber (T300)
End caping	Aluminum alloy	Filled blocks between PM	Aluminum alloy
Winding insulation material	Polyimide film and PTFE	Winding insulation material	Polyimide film and PTFE
-	-	Clamping ring	Aluminum alloy



(a) The 3D model



(b) The axial cross section of rotor

Fig. 9. (Color online) The model of PMSM.

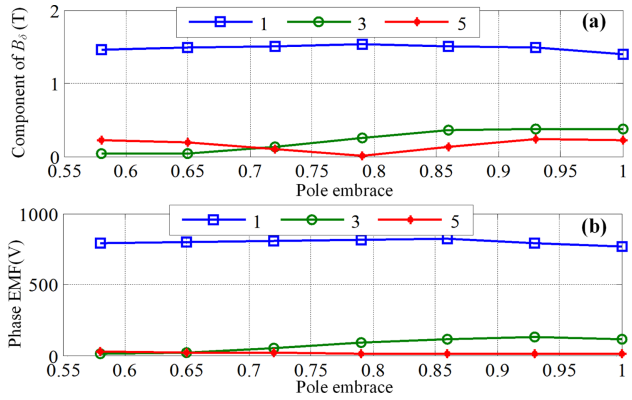
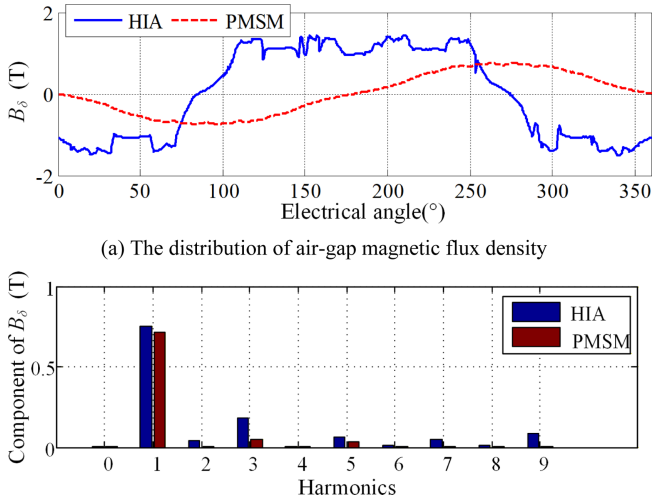


Fig. 10. (Color online) (a) The relationship between the harmonic components of no-load air-gap magnetic field and the pole embrace (b)The relationship between the harmonic components of no-load phase induced voltage and the pole embrace.

When the pole embrace of the PME HIA is set to 0.8, the comparison of air-gap magnetic flux density and harmonic components between the PME HIA and the parallel-magnetized PMSM (with a pole embrace of 0.6),



(a) The distribution of air-gap magnetic flux density

(b) Harmonic components

Fig. 11. (Color online) The comparison of air-gap magnetic flux density and harmonic components for PME HIA and PMSM.

obtained by 3D FEM, is presented in Fig. 11. It should be noted that the effective magnetic flux density for the PME HIA is half the value shown in Fig. 11(a). The results demonstrate that the fundamental component of the air-gap magnetic flux density for the PME HIA is comparable to that of the PMSM. However, the harmonic components of the air-gap magnetic flux density for the PME HIA are larger than those of the PMSM, resulting in correspondingly larger harmonic components in the winding induced voltage. These 3D FEM results are consistent with those of the equivalent 2D model.

6.2. The no-load induced voltage

For the parameters given in Tables 4 and 5, Fig. 12

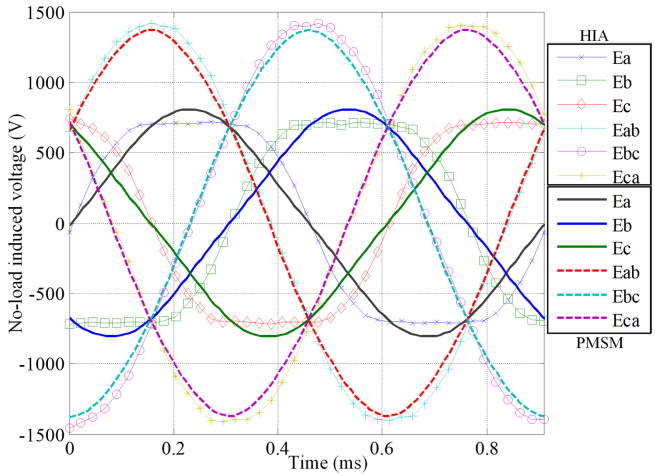


Fig. 12. (Color online) The simulated waveforms of no-load induced voltage for PME HIA and PMSM.

presents the simulated waveforms of the no-load induced voltage for the PME HIA and the parallel-magnetized PMSM. It can be observed that, for the phase voltage, the harmonic content of the no-load induced voltage for the PMSM is significantly smaller than that of the PME HIA. This is because the 3rd harmonic components of the air-gap magnetic flux density for the PME HIA are larger than those of the PMSM. In contrast, for the line-to-line voltage, the harmonic content of the no-load induced voltage for the PMSM is comparable to that of the PME HIA, as the 3rd harmonic is eliminated in the line-to-line voltage.

7. Comparison of power density

Because the pole embrace is typically selected in the range of 0.6–0.8, and the results presented in the previous section demonstrate that the pole embrace has negligible impact on the fundamental component of the air-gap magnetic field, the power density can be considered approximately proportional to the amplitude of the air-gap magnetic flux density.

From the 2D model of the PME HIA, and noting that the magnetic flux density is the sum of the left and right components, the equivalent amplitude of the air-gap magnetic flux density is expressed as:

$$B_{\delta e} = \frac{B_\delta}{2} = \frac{l_m B_m}{2\mu_r \delta} \frac{R_\delta}{2R_\delta + R_m} \tag{6}$$

For the PMSM, the amplitude of air-gap magnetic flux density is:

$$B_\delta = \frac{h_M B_m}{\mu_r \delta k_\delta} \tag{7}$$

Here, k_δ represents the Carter's coefficient of the stator, h_M denotes the magnet thickness, and δ is the equivalent air-gap length, which includes the magnet thickness. Since h_M is typically approximately 2/3 of the equivalent air-gap length, the amplitude of the air-gap magnetic flux density for the PMSM is approximately 0.7–0.75 T. For the PME HIA, the calculation results presented in [27] demonstrate that a larger $B_{\delta e}$ corresponds to a lower machine mass. From (6), it can be seen that when magnetic circuit saturation is neglected, $B_{\delta e}$ can readily exceed 0.75 T by selecting a sufficiently large l_m. The maximum air-gap magnetic flux density is approximately 1.5 T, which is constrained by the saturation flux density of the rotor material; consequently, the maximum value of $B_{\delta e}$ is approximately 0.75 T. Therefore, the analytical analysis leads to the conclusion that the amplitude of the air-gap magnetic flux density for the PME HIA and PMSM is comparable. Because the power density of an electrical machine is proportional to the amplitude of the air-gap magnetic field, the power density of the PME HIA is approximately equivalent to that of the PMSM.

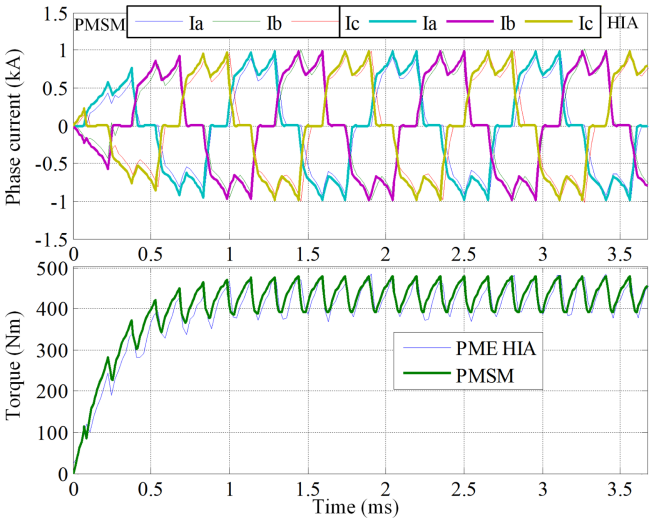


Fig. 13. (Color online) The simulated waveforms of phase currents and torque at rated load for PME HIA and PMSM.

For the parameters given in Tables 4 and 5, the results presented in the previous section demonstrate that the fundamental components for the PME HIA and PMSM are equivalent. The torque waveforms at rated load for the PME HIA and PMSM are shown in Fig. 13. It can be observed that the average torque and current amplitude for both machines are very close. However, the torque ripple of the PME HIA is larger than that of the PMSM, with values of 12.4% and 10.4%, respectively. This is attributable to the fact that the harmonic content of the no-load induced voltage for the PMSM is smaller than that of the PME HIA. Consequently, the FEM simulation results indicate that the power of the two machines is approximately equivalent. For the designed PME HIA and PMSM, the mass of the PMSM is slightly smaller than that of the PME HIA, at 235 kg and 240 kg, respectively. Therefore, the design results also confirm that the power density of the PME HIA is comparable to that of the PMSM.

8. Comparison of reaction and leakage inductance

The calculation of the *d*- and *q*-axis synchronous inductances for the PME HIA can be performed using the methods established for salient-pole synchronous machines. For a detailed derivation, the reader is referred to [31].

The air-gap permeance employed in the analytical approach is obtained from a look-up table, which is generated using a two-dimensional FEM simulation model as described in [31] and [32].

In the calculation of the *d*-axis synchronous inductance, the magnetic potential drop across the permanent magnet is also taken into account. Owing to this magnetic potential drop in the permanent magnet, the *d*-axis synchronous inductance is smaller than the *q*-axis synchronous inductance.

The analytical formulas for the reaction inductance of the PME HIA are given as follows [31]:

$$\begin{aligned} L_{md} &= k_{sd}\frac{6\mu_0 D_i l_{ef}}{\delta\pi}\left(\frac{Nk_N}{p}\right)^2\left(\lambda^*_0+\frac{\lambda^*_2}{2}\right) \\ L_{mq} &= k_{sq}\frac{6\mu_0 D_i l_{ef}}{\delta\pi}\left(\frac{Nk_N}{p}\right)^2\left(\lambda^*_0-\frac{\lambda^*_2}{2}\right) \end{aligned} \tag{8}$$

Here l_{ef} is the effective length, λ^*_0 and λ^*_2 and represents the per-unit values of the DC and second harmonics component of air-gap permeance respectively, k_{sd} and k_{sq} is the saturation factor for *d*- and *q*-axis reaction inductance, and μ_0 is the permeability of vacuum. Usually, the λ^*_0 is approximately to 0.5, and λ^*_2 is small. When the RMS value of winding EMF and the amplitude of air-gap magnetic flux density is fixed, it can be obtained that:

$$D_i l_{ef} N = K \tag{9}$$

Here, *K* is constant. Then it can be obtained that:

$$\begin{aligned} L_{mq} &\approx k_{sd}\frac{3\mu_0 NK}{2\delta\pi}\left(\frac{k_N}{p}\right)^2 \\ L_{mq} &\approx k_{sq}\frac{3\mu_0 NK}{2\delta\pi}\left(\frac{k_N}{p}\right)^2 \end{aligned} \tag{10}$$

It can be observed that the air-gap length and the series turn number per phase have a significant impact on the reaction inductance. The calculation formulas for the PMSM are similar to those for the PME HIA, with the equivalent air-gap length including the magnet thickness.

The comparison of reaction inductance can also be interpreted using the 2D model. For the PME HIA, the reaction inductance of Part 2 in the 2D model can be neglected, and the rotor of Part 1 can be approximated as a smooth rotor. Under this condition, the PME HIA can be regarded as equivalent to a surface-mounted PMSM. Therefore, when the fundamental component of the air-gap magnetic flux density is equal for both the PME HIA and the PMSM, the ratio of reaction reactance is approximately expressed as:

$$k_{L_m} \approx \frac{\delta_{PMSM}}{2\delta_{HIA}}\frac{N_{HIA}}{N_{PMSM}} \tag{11}$$

Here, the δ_{PMSM} and δ_{HIA} are the air-gap length for PMSM and PME HIA respectively, and N_{PMSM} and N_{HIA} are the series turn number per phase for PMSM and PME HIA respectively.

3D FEM simulations are employed to validate the analytical calculations. The simulation conditions are as follows. Magnetic circuit saturation is taken into account during the simulation, with the A-phase winding current set to its rated value. The *d*- and *q*-axis synchronous reactances are calculated from the ratio of the EMF to the current of Phase A, and the synchronous inductance is subsequently derived from the synchronous reactance.

For the parameters given in Tables 4 and 5, Table 7 presents a comparison between the synchronous inductances obtained from analytical calculations and FEM simulations. The analytical results are in good agreement with the FEM simulation results. The comparison of reaction and leakage inductances is presented in Table 8. It can be seen that, for the PME HIA, the reaction inductance is significantly larger than the leakage inductance. The corresponding results for the PMSM are also included in Tables 7 and 8. It can be observed that the synchronous inductance of the PME HIA is substantially larger than that of the PMSM. This is attributable to the fact that the reaction inductance of the PME HIA is much

Table 7. Comparison of analytical calculation and FEM simulation for synchronous inductance.

Parameters	Analytical	FEM simulation
HIA		
Synchronous inductance of *d* axis (μH)	44	41.5
Synchronous inductance of *q* axis (μH)	57	54
PMSM		
Synchronous inductance of *d* axis (μH)	33.1	33.5
Synchronous inductance of *q* axis (μH)	33.1	33.5

Table 8. Comparison of reaction and leakage inductance.

Parameters	Reaction	Leakage
HIA		
Inductance of *d* axis (μH)	34.5	7
Inductance of *q* axis (μH)	47	7
PMSM		
Inductance of *d* axis (μH)	10.7	22.4
Inductance of *q* axis (μH)	10.7	22.4

larger than that of the PMSM, which results from its considerably smaller air-gap length. In contrast, the leakage inductance of the PME HIA is much smaller than that of the PMSM, owing to its slotless stator-core structure.

9. Comparison of losses and efficiency

The losses of the PME HIA and PMSM mainly comprise air friction losses, mechanical losses, stator iron core losses, rotor eddy-current losses, and armature winding copper losses. The air friction losses for both machines are calculated using empirical formulas from [16], which have been validated by experimental results. The stator iron core losses and rotor eddy-current losses are computed through 3D or 2D FEM simulations. Table 9 summarizes the calculated losses for the PME HIA and PMSM under rated load conditions.

It is evident that the armature copper losses and stator iron core losses of the PME HIA are significantly lower than those of the PMSM. Conversely, the rotor eddy-current losses and air friction losses of the PME HIA are considerably higher than those of the PMSM.

9.1. Winding copper losses

When non-Litz wire is employed, the slotless stator core structure of the PME HIA alleviates the severe squeezing effects on the armature winding. The simulation model for winding copper losses, accounting for squeezing effects, is presented in Fig. 14. This model aims to analyze the impact of squeezing effects on copper losses in the winding. To account for eddy-current effects, the winding is modeled as a "solid" conductor in the software, enabling the calculated winding copper losses to include both eddy-current losses and static ohmic losses. The conductor cross-sectional area for the PME HIA winding is 52 mm², with 13 sub-conductors. For the PMSM winding, the cross-sectional area is 40 mm², with three parallel branches. It is assumed that the current in each conductor is one-third of the total phase current. The simulation results indicate that the winding copper losses are 4.3 kW and 26.0 kW for the PME HIA and PMSM, respectively. It should be noted that temperature affects the squeezing effects in the armature winding. Non-uniform temperature distribution within the winding can actually help alleviate these squeezing effects. However, this temperature non-uniformity was neglected in the simulation to simplify the analysis.

Analytical calculation formulas from [33-35] can also be employed to compute winding copper losses considering squeezing effects. Furthermore, skin effects in the winding end region can be calculated using the analytical formulas presented in [36].

The current density of the PME HIA winding is approximately 12 A/mm², while that of the PMSM winding is approximately 5.2 A/mm². Although the current density of the PME HIA winding is higher than that of the PMSM winding, the winding copper losses of the PME

Table 9. Different kinds of losses for HIA and PMSM under rated load.

	PME HIA	PMSM
Stator iron core losses (kW)	2.5	14.2
Rotor eddy-current losses (kW)	6	0.35
Mechanical and air friction losses (kW)	6.4	0.17
With Litz wire		
End winding copper losses (kW)	1.4	2.2
Effective-part winding copper losses (kW)	1.5	2.6
Total losses (kW)	17.8	19.52
Efficiency	98.3%	98.1%
With non-Litz wire		
End winding copper losses (kW)	1.4	1.0
Effective-part winding copper losses (kW)	2.9	25.0
Total losses (kW)	19.2	40.72
Efficiency	98.1%	96.1%

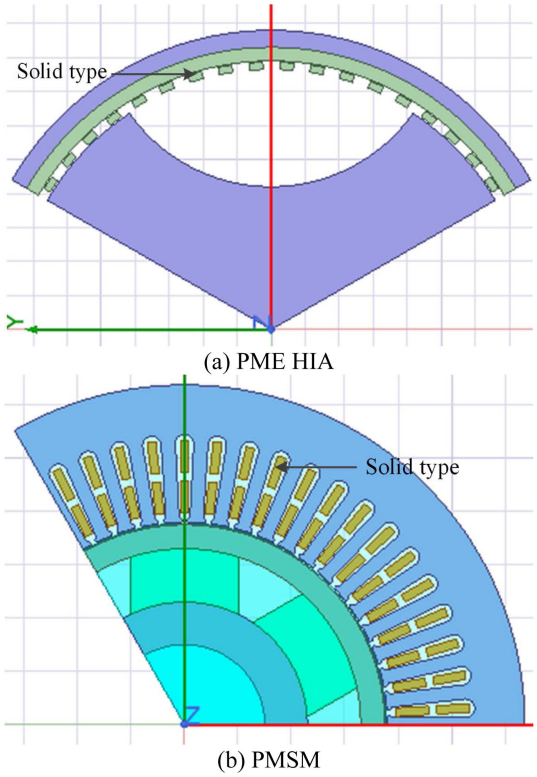


Fig. 14. (Color online) The simulation model for winding copper losses of effective parts considering squeezing effects.

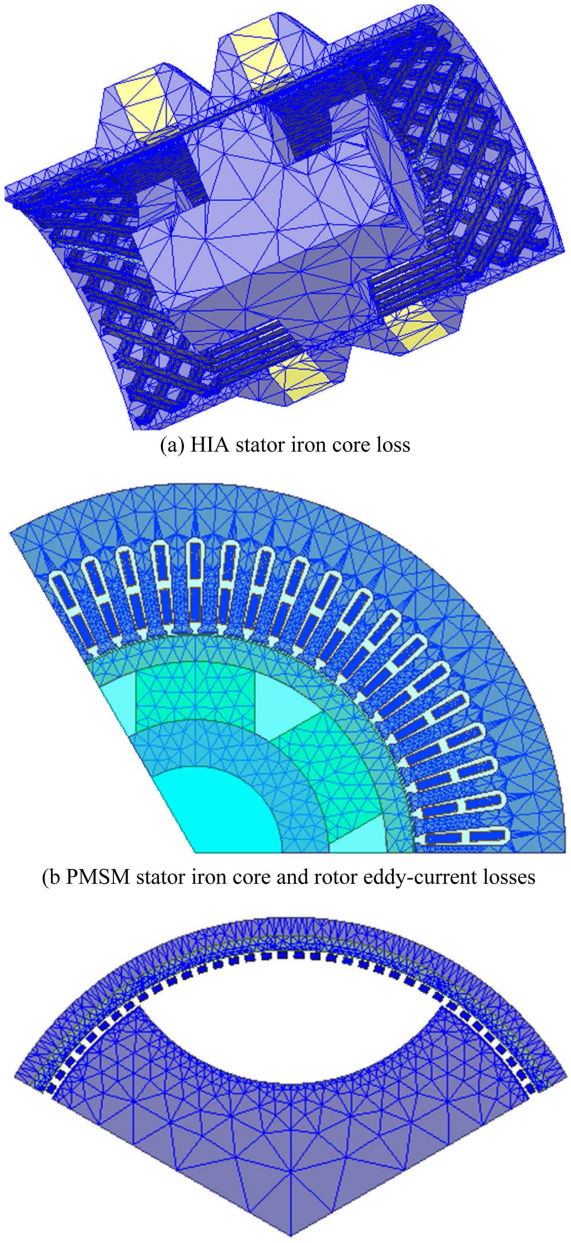
HIA are substantially lower than those of the PMSM. This is because the extremely severe squeezing effects on the armature winding are alleviated in the PME HIA due to its slotless stator-core structure, which is the same as the slotless PMSM [9,10].

When Litz wire is employed, the comparison of winding copper losses is also presented. Litz wire can dramatically reduce copper losses for the PMSM [4-5], and the copper losses of the PME HIA are also significantly lower than those of the PMSM. This is attributable to the slotless stator-core structure, which facilitates the insertion of Litz wire, resulting in a much higher slot fill factor for the PME HIA compared with the PMSM.

9.2. Stator iron core losses

The 3D FEM model and the 2D FEM model as shown in Figs. 15(a) and 15(b), combined with external control circuits, are employed to simulate the stator iron core losses for the PME HIA and PMSM, respectively. The element numbers for the PME HIA and PMSM models are 83,217 and 14,587, respectively, with required simulation times of approximately 2 hours and 0.5 hours, respectively.

The simulated stator iron core losses for the PMSM and PME HIA are presented in Table 9 and Fig. 16. The stator iron core losses of the PME HIA are 2.5 kW, whereas those of the PMSM are 14.2 kW. This difference arises because stator iron core losses are proportional to the square of the magnetic flux density. In the PMSM, the slotted stator core structure results in higher magnetic flux density in the teeth. In contrast, the slotless stator core of the PME HIA yields a relatively uniform magnetic flux density. Additionally, the mass of the PMSM stator core is significantly larger than that of the PME HIA, at 80 kg and 15 kg, respectively. This difference is due to the considerably smaller thickness of the stator iron yoke in the PME HIA. The magnetic fluxes in the PME HIA pass through the shell and then the other half of the stator core; consequently, there is no requirement for a stator iron yoke to carry magnetic fluxes between adjacent poles.



(a) HIA stator iron core loss

(b PMSM stator iron core and rotor eddy-current losses

(c) HIA rotor eddy-current loss

Fig. 15. (Color online) The simulation model of stator iron core losses and rotor eddy-current losses for PME HIA and PMSM.

9.3. Rotor eddy-current losses

Because the element number of a 3D FEM model would become excessively large if the rotor were meshed with very fine quality, resulting in simulation times of several hours, the 3D FEM model is not employed for rotor eddy-current loss calculations. Instead, the single-sided rotor 2D FEM model from our previous study [16], as shown in Fig. 15(c), is used to simulate the rotor eddy-current losses for the PME HIA. The current excitation is obtained from the simulation results of the 3D FEM model combined with the external control circuit. For the PMSM, a 2D FEM model combined with the external control circuit is employed.

To ensure accurate simulation of rotor eddy-currents losses, the rotor face meshes for both the PME HIA and PMSM are refined, as shown in Figs. 15(b) and 15(c). The element number for the PME HIA 2D FEM model is 8,270, with a required simulation time of approximately 6 minutes.

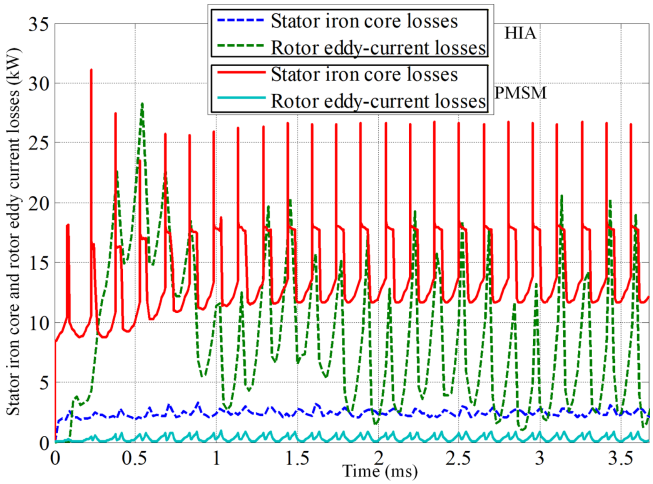


Fig. 16. (Color online) The simulated waveforms of stator iron core losses and rotor eddy-current losses and at rated load for PME HIA and PMSM.

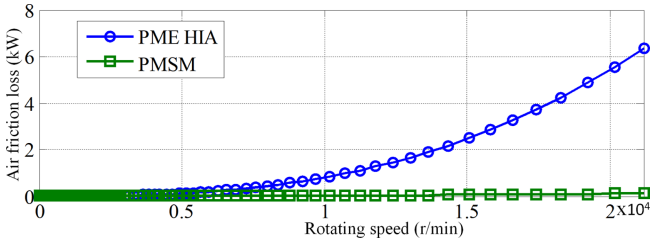


Fig. 17. (Color online) The calculated air friction losses for PME HIA and PMSM.

The simulated rotor eddy-current losses for the PME HIA and PMSM are presented in Fig. 16. The rotor eddy-current losses of the PMSM are 0.35 kW, whereas those of the PME HIA are 6 kW. This difference is attributable to the axial magnet segmentation in the PMSM, which dramatically reduces eddy currents.

9.4. Air friction losses

The air friction losses for the PME HIA and PMSM, calculated using the empirical formulas presented below [16], are shown in Fig. 17.

$$P_{wind} = \frac{1}{16} C_{fs0} \pi p_{air} D^4 \omega^3_r l \tag{12}$$

Here, C_{fs0} is the skin friction coefficient, ρ_{air} is the density of air, ω_r is the rotor angular speed in rad/s, D is the diameter of rotor, and l is the length of rotor. The skin friction coefficient has a relationship with the Reynolds number R_e as follows [37].

$$C_{fs0} = \frac{2}{R_e}, R_e < 1100 \tag{13}$$

$$1/\sqrt{C_{sf0}} = B + 1.768 \ln(R_e \sqrt{C_{sf0}}), R_e \geq 1100 \tag{14}$$

where B is a constant determine by the experimental results, to be 2.04 [37]. For PME HIA, the effects of the salient structure on the windage losses can be simplified by multiplying a constant [37], which is defined by the following equation:

$$K_{\text{wind}} = 17(h/D) + 2.2 \tag{15}$$

Here, h is the rotor slot depth.

At a rotational speed of 22,000 r/min, the air friction losses for the PMSM and PME HIA are 0.12 kW and 6.3 kW, respectively, as shown in Fig. 17. The air friction losses of the PME HIA are substantially higher than those of the PMSM. This difference is attributable to the significantly higher rotor tip speed of the PME HIA compared with that of the PMSM. Additionally, the PME HIA features a salient rotor structure, whereas the PMSM has a smooth rotor outer surface.

10. Comparison of temperature rising

The simulation conditions for the PME HIA are as follows: the machine operates at rated load, with a rotational speed of 22,000 r/min and an output power of 1,000 kW. Under these conditions, the losses are calculated using the methods presented in the preceding sections.

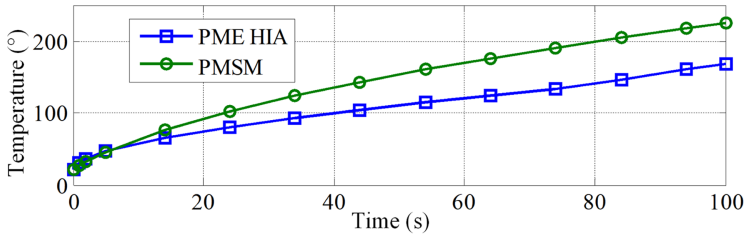
The simulation conditions for the PMSM are identical to those of the PME HIA. Both machines employ water cooling at the casing, with the same surface heat transfer coefficient and ambient temperature. The thermal properties of the materials for both machines are summarized in Table 10.

10.1. Non-Litz Wire Case

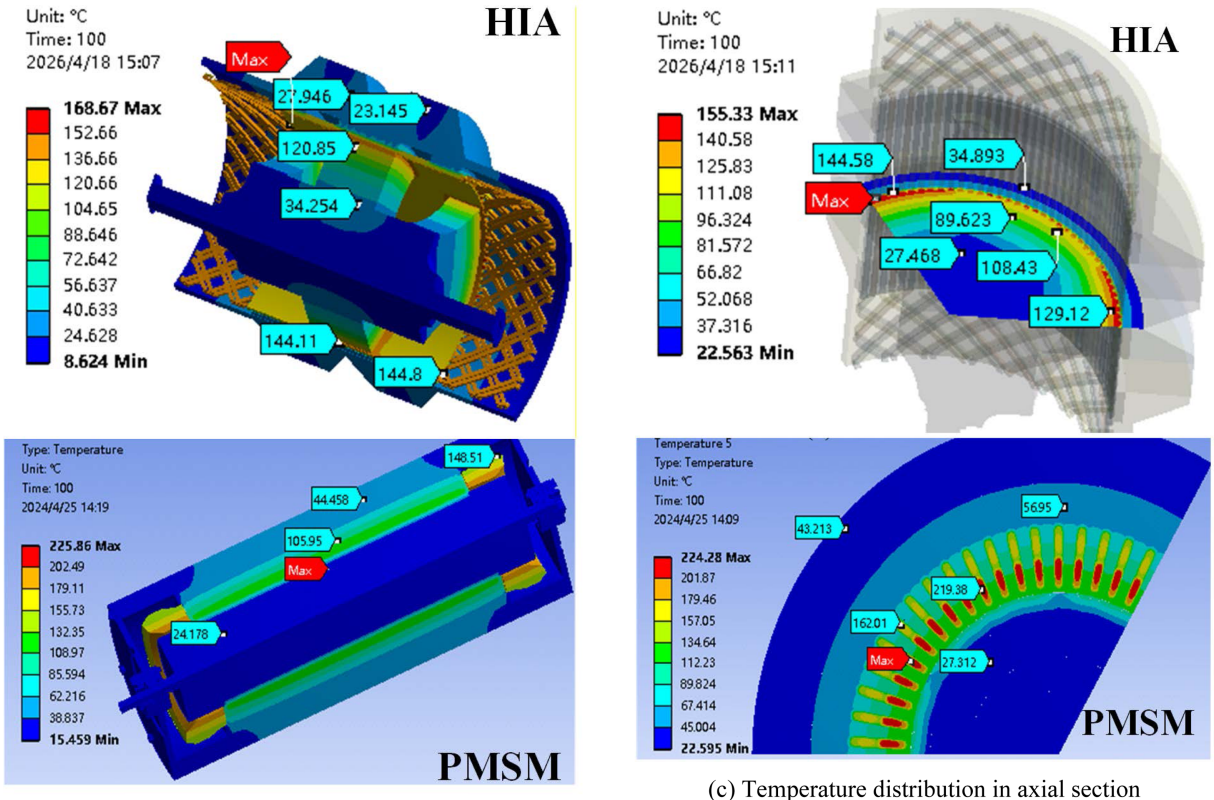
When non-Litz wire is employed, the winding copper losses are 1.0 kW and 25 kW for the end winding and effective parts of the PMSM, respectively, and 1.4 kW and 2.9 kW for the end winding and effective parts of the PME HIA, respectively. The temperature rise curves for the maximum temperature of the PME HIA and PMSM are shown in Fig. 18(a), while the 3D temperature distribution at 100 s is presented in Fig. 18(b). The temperature distribution in the axial section is shown in Fig. 18(c). The simulation results indicate that the maximum temperature at 100 s reaches approximately 225 °C for the PMSM, occurring in the effective part of the winding. It can also be observed that the temperature rise of the PMSM is significantly higher than that of the PME HIA.

Table 10. The thermal properties parameters of materials for PME HIA and PMSM.

Parameters	Specific heat capacity J/(kg·°C)	Thermal conductivity (W/(m·K))	Mass density (kg/m^3)
40CrNiMoA	460	44.5	7830
DW-310-35	460	Radial: 29.1; Axial: 0.7	7650
Q235	434	60	7800
Magnet	470	9	7500
Aluminum alloy	900	230	2770
Copper	390	Radial: 1.3; Axial: 343	8900
Epoxy resin	550	0.2	3100
Carbon fiber	760	0.5	1760
Air	1000	0.026	1.16
Air in air-gap	1000	0.5	1.16
Bearing	470	Radial: 0.5; Axial: 47	7800



(a) The temperature rising curve



(b) 3D temperature distribution

(c) Temperature distribution in axial section

Fig. 18. (Color online) Temperature results calculated by FEM for PME HIA and PMSM with non-Litz wire.

Furthermore, for the armature winding of the PMSM, the temperature of the end winding is considerably lower than that of the effective parts, as the skin effects are much less severe in the end winding region.

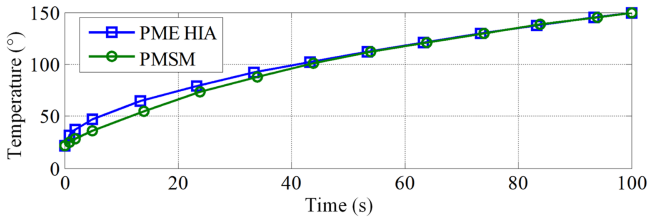
10.2. Litz Wire Case

When Litz wire is employed, the winding copper losses are 2.2 kW and 2.6 kW for the end winding and effective parts of the PMSM, respectively, and 1.4 kW and 1.5 kW for the end winding and effective parts of the PME HIA, respectively. The temperature rise curves for the maximum temperature of the PME HIA and PMSM are shown in Fig. 19(a), while the 3D temperature distribution at 100 s is presented in Fig. 19(b). The temperature distribution in the axial section is shown in Fig. 19(c). It can be observed that Litz wire dramatically reduces the temperature rise of the winding effective parts; however, it increases the temperature rise of the end winding.

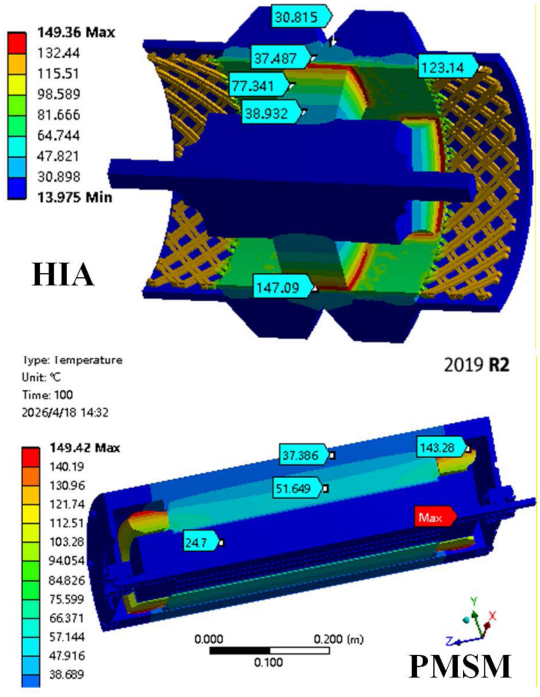
The parameters for the winding insulation materials (polyimide film and PTFE) are presented in Table 11. The comparison of thermal safety margins for the PME HIA and PMSM is shown in Table 12. It can be seen that the PME HIA exhibits substantially larger thermal safety margins than the PMSM for both cases, with and without Litz wire.

11. Comparison of rotor structure safety

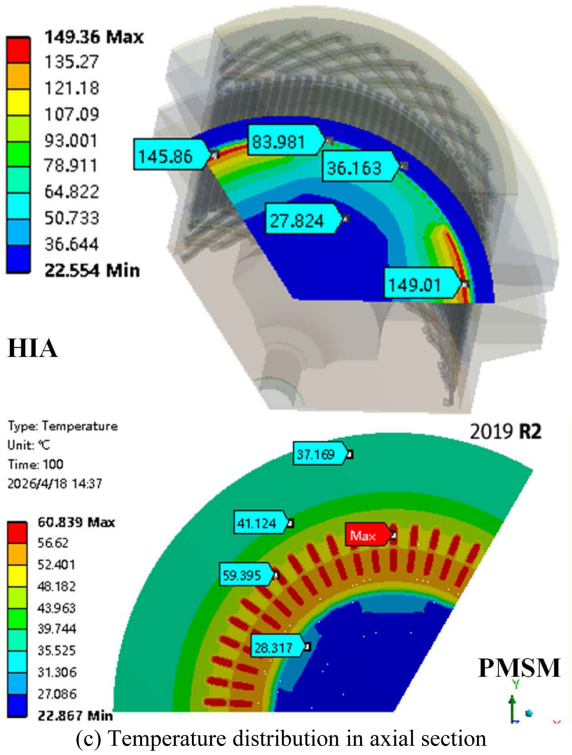
The parameters of the rotor materials for the FEM-based stress and dynamic analyses are presented in Table 13. For the PMSM, cases with interference fits of 0.1 mm, 0.2 mm, and 0.3 mm, and rotational speeds of 0 and 22,000 r/min are considered. When the interference is 0.3 mm and the rotational speed is 22,000 r/min, the von Mises stress distribution of the PMSM rotor is shown in Fig. 20(a), while the magnet radial stress is presented in Fig. 20(b). It can be observed that the maximum stress occurs in the sleeve, with a value of 1,057 MPa, which is



(a) The temperature rising curve



(b) 3D temperature distribution



(c) Temperature distribution in axial section

Fig. 19. (Color online) Temperature results calculated by FEM for PME HIA and PMSM with Litz wire.

Table 11. Parameters for winding insulation material of polyimide film and PTFE.

Parameters	Polyimide film	PTFE
Maximum allowable temperature (°C)	250	260
Breakdown field strength	210 kV/mm	200 kV/mm
Thickness	0.025-0.035 mm	0.01-0.05 mm

Table 12. Comparison of thermal safety margins for PME HIA and PMSM.

Components	End winding insulation material	Carbon fiber	PM	Effective-part winding insulation material	Rotor core
Maximum allowable temperature (°C)	250	150	180	250	PME HIA: 743, PMSM: 150
With Litz wire					
PME HIA temperature (°C)	125	-	20	90	150
PME HIA (%)	100	-	800	178	395
PMSM temperature (°C)	150	50	25	60	25
PMSM (%)	67	200	620	317	500
With non-Litz wire					
PME HIA temperature (°C)	156	-	20	130	153
PME HIA (%)	60	-	800	92	385
PMSM temperature (°C)	175	90	30	225	30
PMSM (%)	30	67	500	11	400

Table 13. The mechanical performance parameters of rotor materials for PME HIA and PMSM.

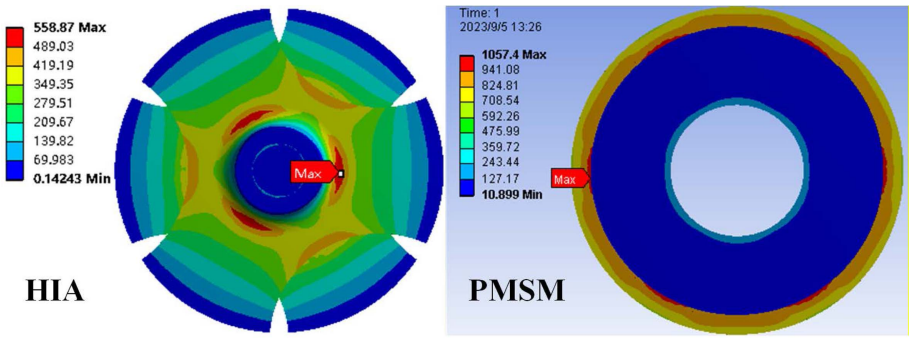
Parameters	40CrNiMoA	Carbon fiber	Magnet	Aluminum alloy	DW-310-35
Elastic modulus (GPa)	209	Circumferential: 230 Radial: 10	150	71	200
Poisson's ratio	0.3	Circumferential: 0.3 Radial: 0.18	0.29	0.33	0.3
Mass density (kg/m^3)	7830	1760	7500	2770	7650
Strength (MPa)	980	Circumferential: 3530 Radial: 400	Compressive: 900 Tensile: 80	250	410
Coefficient of thermal expansion (10^{-6} m.K^{-1})	11.7	Circumferential: 0.02 Radial: 22.5	9	22	11.6

significantly lower than the tensile strength of carbon fiber T300. The radial stress in the magnet is negative, indicating that the magnet is under compression by the sleeve; the maximum radial stress is approximately 160 MPa, which is considerably lower than the compressive strength of the magnet. For comparison, the von Mises stress of the PME HIA rotor is also shown in Fig. 20(a); the tensile strength of the alloy steel is approximately 980 MPa.

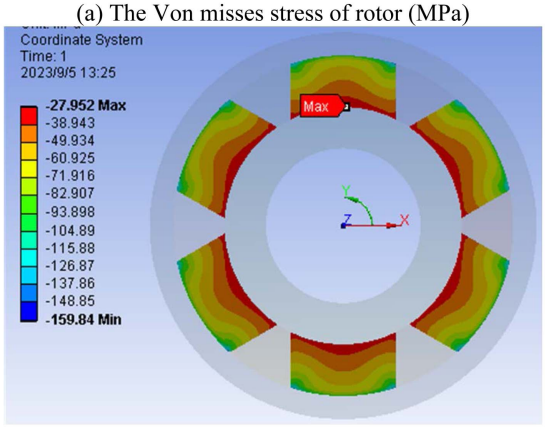
The rotor component stresses for the PMSM with different interference fits are summarized in Table 14. The simulation results indicate that an interference of 0.2 mm is optimal, as this condition maximizes the stress safety factors for all rotor components. The comparison of rotor component stresses for the PMSM with and without temperature rise, at an interference of 0.2 mm and a rotational speed of 22,000 r/min, is presented in Table 15. It can be observed that temperature rise has negligible effects on the stress. The comparison of mechanical safety margins for the PME HIA and PMSM is shown in Table 16. It can be seen that the mechanical safety margins for the PME HIA are also larger than those of the PMSM.

The bearing parameters for the PME HIA and PMSM are presented in Table 17. The bearing selection accounts for the required load capacity and rotational speed limits. The bearing diameter for the PMSM is selected to ensure that the first critical speed of the rotor is sufficiently distant from the rated speed of 22,000 r/min.

The simulated first and second critical speeds of the



(a) The Von misses stress of rotor (MPa)



(b) The magnet radial stress (MPa)

Fig. 20. (Color online) The rotor stress results calculated by FEM for PME HIA and PMSM.

Table 14. Rotor component stress (MPa) for PMSM with different interferences.

Components	Rotor core	Rotor sleeve	PM	Filled blocks between PM
0.1 mm@ 0 r/min	130	Mises: 300 Radial: -87 Circumferential:282	Outer position: -38 Inner position: -19	29
0.1 mm@ 22000 r/min	86	Mises: 493 Radial: -218 Circumferential: 475	Outer position: -101 Inner position: 0	30
0.2 mm@ 0 r/min	249	Mises: 605 Radial: -174 Circumferential: 570	Outer position: -77 Inner position: -35	56
0.2 mm@ 22000 r/min	20	Mises: 749 Radial: -233 Circumferential:700	Outer position: -114 Inner position: -9	53
0.3 mm@ 0 r/min	377	Mises: 916 Radial: -256 Circumferential: 867	Outer position: -125 Inner position: -54	81
0.3 mm@ 22000 r/min	141	Mises: 1057 Radial: -312 Circumferential: 992	Outer position: -160 Inner position: -28	78

PMSM rotor shaft are approximately 10,000 r/min and 30,000 r/min, respectively, as shown in Fig. 21(a). The second bending mode of the PMSM rotor shaft and the first bending mode of the HIA rotor are shown in Fig. 21(b). Although both the first and second critical speeds are distant from the maximum operating speed of 22,000 r/min in the high-speed drive system, the separation margin percentage for the second critical speed is 36%,

Table 15. Comparison of rotor component stress (MPa) for PMSM with and without temperature rising when interference is 0.2 mm and rotating speed is 22000 r/min.

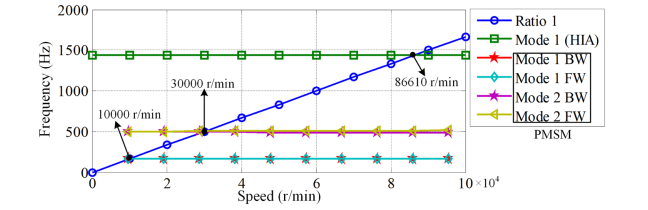
Components	Rotor core	Rotor sleeve	PM	Filled blocks between PM
Without temperature rising	20	Mises: 749 Radial: -233 Circumferential:700	Outer position: -114 Inner position: -9	53
With temperature rising	20	Mises: 750 Radial: -254 Circumferential: 704	Outer position: -113 Inner position: -10	52

Table 16. Comparison of mechanical safety margins for PME HIA and PMSM.

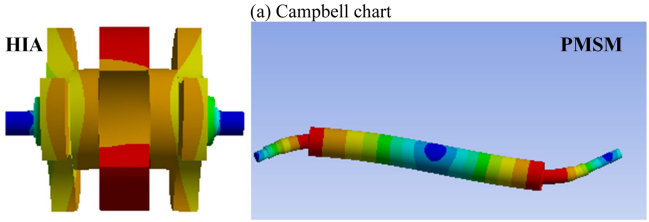
Parameters	Rotor core strength	Rotor sleeve strength	PM strength	Filled blocks strength
PME HIA	75%	-	-	-
PMSM	64%	Circumferential: 404%, Radial: 72%	689%	346%

Table 17. Parameters of bearing for PME HIA and PMSM.

Parameters	Specification	Inner diameter	Required load	Rated dynamic load	Load safety margin	Grease lubrication limit speed	Speed safety margin
PME HIA	NSK 71908C HQ1 (Dual)	40 mm	8000 N	16000 N	100%	42000 r/min	91%
PMSM	GMN HY KH 6006 C TA	30 mm	1500 N	8200 N	447%	62500 r/min	184%



(a) Campbell chart



(b) First (for HIA rotor) and Second (for PMSM rotor shaft) band modal

Fig. 21. (Color online) The simulated results for modal and Campbell chart for PME HIA and PMSM.

which is significantly lower than that of the PME HIA, as presented in Fig. 21(a). The comparison of critical speed safety margins for the PME HIA and PMSM is shown in Table 18. It can be seen that both the PMSM and HIA satisfy the IEC 60034-14 requirement.

12. Comparison of linearity of relationship between torque and current

The results presented in the previous section demonstrate that the reaction inductance of the PME HIA is significantly larger than that of the PMSM. This implies

Table 18. Comparison of critical speed safety margins for PME HIA and PMSM.

Parameters	Critical speed
PME HIA	294%
PMSM	36%

that the armature reaction of the PME HIA may be considerably stronger than that of the PMSM, potentially leading to more severe core magnetic saturation. The simulated relationship between torque and phase current is shown in Fig. 22, where both torque and current are normalized to their respective rated values. The simulation results indicate that the torque-current linearity for both the PME HIA and PMSM is satisfactory, although it is superior for the PMSM. The satisfactory linearity of the PME HIA is attributable to its slotless stator structure, which renders the stator iron core less susceptible to saturation. Furthermore, because the maximum current is constrained by thermal insulation limits, the armature reaction has a limited impact on magnetic saturation.

To improve the linearity of the PME HIA, lead angle control can be employed, as shown in Fig. 22, the linearity with lead angle is better. Additionally, selecting a larger effective air-gap length and utilizing high-saturation materials such as 1J22 alloy can reduce saturation effects [38]. The topology employing PM excitation in the rotor slot [39] can also be adopted to improve linearity and power density.

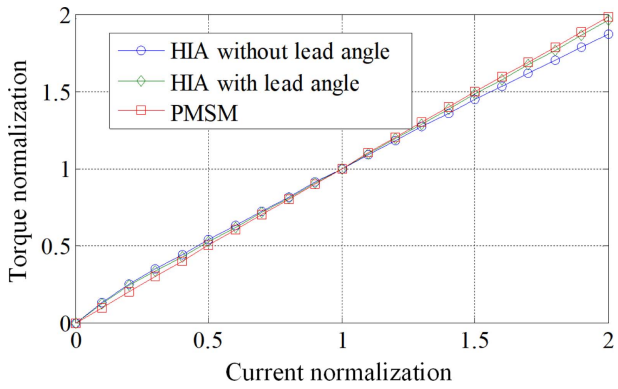


Fig. 22. (Color online) The relationship between torque and current.

13. Comparison of Reliability and Manufacturing Difficulty

The rotor structure of the PMSM is complex, whereas the rotor of the PME HIA is simple and highly reliable. The rotor stress in the PMSM is intricate because it is coupled with temperature, which varies during machine operation. This complicates accurate rotor stress analysis and makes it difficult to ensure absolute rotor safety under complex operating conditions.

In contrast, the magnets in the PMSM exhibit eddy-current losses, and under poor heat dissipation conditions, the temperature rise of the magnets and sleeve can become very high, potentially causing demagnetization and carbon fiber sleeve failure. However, in the PME HIA, the magnet is positioned between two half-shells, ensuring nearly constant magnetic flux density and minimal eddy-current losses. Furthermore, the heat dissipation conditions for the magnet in the PME HIA are significantly superior to those in the PMSM. Consequently, the magnet temperature in the PME HIA remains very low, with no risk of demagnetization. Although the simulation results indicate a small temperature rise for the PMSM magnet, the simulation duration is short. Under repetitive operating conditions, heat accumulation in the magnet may lead to a substantial temperature rise due to the inferior heat dissipation conditions of the PMSM rotor.

Therefore, it can be concluded that the PME HIA offers substantially higher reliability than the PMSM. Additionally, owing to its slotless stator-core structure, the insertion of Litz wire in the PME HIA is considerably easier than in the PMSM. The fabrication of rotor for PME HIA is much easier than that of PMSM. So, manufacturing difficulty for PME HIA is also smaller than the PMSM.

14. Verification of 2D FEM model for PME HIA

Our previous study [40] demonstrated that the effects of axial magnetomotive force drop on the winding inductance can be modeled using an equivalent rotor with different air-gap length and rotor slot width. Subsequently, the 2D FEM model for the 3D model with equivalent rotor can be established using the method introduced in the preceding section. The 3D FEM simulation is employed to validate the 2D FEM model. The comparison of the relationships between the harmonic components of no-load air-gap magnetic field, induced voltage, and pole embrace simulated by 3D and 2D FEM for the PME HIA is shown in Fig. 23. The comparison of synchronous inductance simulated by 3D and 2D FEM for the PME

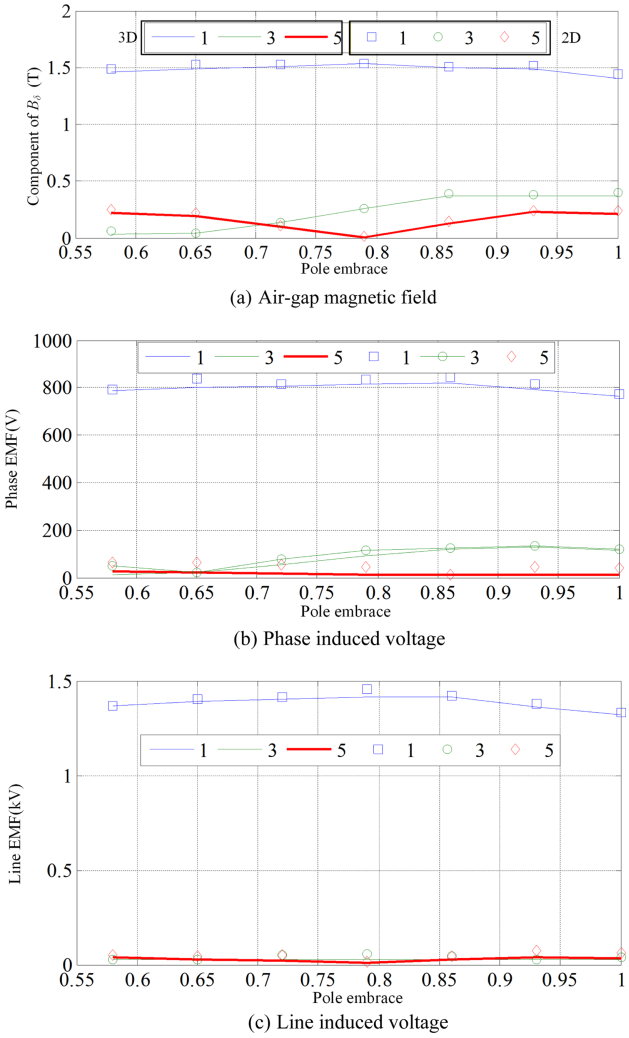
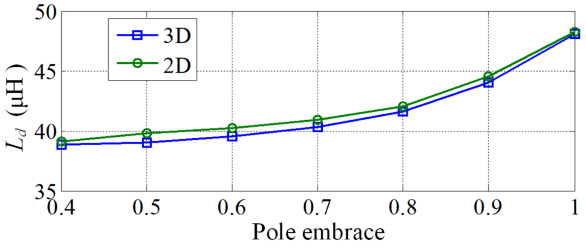
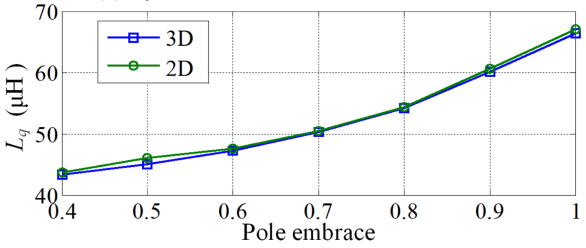


Fig. 23. (Color online) The comparison of relationship between the harmonic components of no-load air-gap magnetic field, induced voltage and the pole embrace simulated by 3D and 2D FEM for PME HIA.



(a) Synchronous inductance of *d*-axis



(b) Synchronous inductance of *q*-axis

Fig. 24 (Color online) The comparison of synchronous inductance simulated by 3D and 2D FEM for PME HIA.

HIA is presented in Fig. 24. The simulation results indicate that the 2D and 3D FEM simulation models are in good agreement. By comparing Figs. 5, 7, 8, and 23, it can be observed that although neglecting the variation of PM thickness in 2D FEM model when the pole embrace takes different values has a minor effect on the simulation results for the 2D FEM model, it has negligible impact on the optimal rotor pole embrace.

When the effects of axial magnetomotive force drop on the winding inductance are taken into account, the *d*-axis synchronous inductance may be smaller or larger than the *q*-axis synchronous inductance depending on the pole embrace value; consequently, the slot width coefficient for the equivalent rotor of the 3D model would be smaller than, equal to, or larger than 0.5. When the *d*-axis synchronous inductance is greater than the *q*-axis synchronous inductance, the PME HIA can be regarded as equivalent to a salient-pole PMSM; when the *d*-axis synchronous inductance is equal to the *q*-axis synchronous inductance, the PME HIA can be regarded as equivalent to a surface-mounted PMSM; when the *d*-axis synchronous inductance is smaller than the *q*-axis synchronous inductance, the PME HIA can be regarded as equivalent to an interior PMSM.

15. Conclusions and future works

15.1. Conclusions

In this paper, an equivalent 2D model for the PME HIA is introduced. The study demonstrates that the PME HIA can be equivalently represented as a salient-pole, surface-mounted, or interior PMSM with radially magnetized permanent magnets, depending on whether the *d*-axis synchronous inductance is greater than, equal to, or less than the *q*-axis synchronous inductance, respectively. The equivalent permanent magnets exhibit significantly higher coercive force; consequently, the magnet thickness in the 2D model is substantially smaller than that in the PMSM. Furthermore, the optimal rotor pole embrace design is identical to that of the radial-magnetized PMSM. For simplified analysis of the air-gap magnetic field, the HIA rotor can be approximated as a smooth rotor in the equivalent 2D model.

A detailed comparison between the PME HIA and PMSM is also presented, with the main conclusions summarized in Table 19.

Both analytical and FEM simulation results demonstrate that the fundamental component of the equivalent air-gap magnetic flux density and the power density of the PME HIA are comparable to those of the PMSM. For the two machines designed in this case study, the power density of the PME HIA is only 2% lower than that of the PMSM. The 3rd harmonic of the no-load air-gap magnetic field and induced phase voltage for the PME HIA is significantly larger than that of the parallel-magnetized PMSM, whereas the other harmonics of the no-load air-gap magnetic field and the line-to-line induced voltage harmonics

Table 19. The conclusion for comparison between PME HIA and PMSM.

Items	PME HIA compared with PMSM
No-load air-gap magnetic field fundamental component	Equivalent
3th harmonic of no-load air-gap magnetic field	Much larger
Other harmonic of no-load air-gap magnetic field	Equivalent
3th harmonic of no-load induced phase voltage	Much larger
Harmonic of line-to-line no-load induced voltage	Equivalent
Power density	Equivalent
Reaction inductance	Much larger
Leakage inductance	Much smaller
Efficiency	2% Higher
Temperature rising	Much Lower
Thermal safety margin	Much larger
Rotor strength safety margin	11% Higher
Separation margin percentage for critical speed	Much larger
Reliability	Much higher
PM usage	Much larger
Linearity between torque and current	Slightly worse
Difficulty of embedding Litz wire	Much lower

are comparable for both machines. Both analytical and FEM simulation results indicate that the reaction inductance of the PME HIA is substantially larger than that of the PMSM due to its considerably smaller equivalent air-gap length, while its leakage inductance is significantly smaller owing to the slotless stator-core structure.

Furthermore, when non-Litz wire is used, the PME HIA achieves higher efficiency, with a 2% improvement compared with the PMSM. The PME HIA exhibits lower armature copper losses and stator iron core losses, although its rotor eddy-current losses and air friction losses are higher than those of the PMSM. The slotless stator-core structure of the PME HIA alleviates squeezing effects on the armature winding, thereby reducing eddy currents in the windings and resulting in significantly lower armature copper losses compared with the PMSM. Moreover, the temperature rise of the PME HIA is substantially lower than that of the PMSM, primarily because the winding copper losses in the effective parts are significantly reduced. When Litz wire is used, the PME HIA has little higher efficiency than PMSM, and the temperature rise of the PME HIA is approximately equal to that of the PMSM. The use of Litz wire in PME HIA is much more convenient than in PMSM. In terms of reliability, the PME HIA surpasses the PMSM due to its simple rotor structure and minimal eddy-current losses in the magnet.

The rotor structural safety and reliability of the PME HIA are significantly higher than those of the PMSM. This study provides valuable guidance for machine selection and enhances the understanding of comparisons between PME HIAs and PMSMs.

15.2. Future Works

The construction of a prototype machine is planned, and experimental tests will be conducted to validate the analytical results presented in this paper. Methods to reduce the harmonics of the no-load air-gap magnetic field and induced voltage, as well as torque ripple, for the PME HIA will be investigated. Possible methods include skewed-pole or skewed-stator configurations, and special rotor shapes such as slotting in the rotor teeth. Additionally, optimal design methods for minimizing synchronous inductance will be investigated in depth.

It should be noted that nonlinear magnetic behavior was neglected when deriving the 2D FEM model for the PME HIA. When nonlinearity is taken into account, it is actually the incremental inductance, rather than the apparent inductance, that influences the dynamic performance of the machine. A 2D FEM model incorporating nonlinear magnetic behavior will be investigated in future work.

Acknowledgement

This work is partially supported by Foundation of Kunming University of Science and Technology (Grant No. KKZ3202404099), Foundation of State Key Laboratory of Advanced Electromagnetic Technology (Grant No. AET 2024KF013), and the Foundation of Yunnan Provincial Department of Science and Technology (Grant No. 202301AS070055).

Declarations

Competing interests

The authors declare that they have no known competing financial interests or personal relationships that could have appeared to influence the work reported in this paper.

References

[1] N. Bernard, R. Missoum, L. Dang, N. Bekka, H. B. Ahmed, and M. E. Zäım, IEEE Trans. Energy Convers. **31**, 477 (2016).
[2] B. Hannon, P. Sergeant, and L. Dupré, IEEE Trans. Magn. **50**, 8101410 (2014).
[3] Z. Y. Jia and B. Kim, International Journal of Electrical and Electronic Engineering & Telecommunication. **7**, 108 (2018).
[4] J. Wang, T. M. Jahns, P. McCluskey, J. Kizito, B. Sarlioglu, R. Borjas, J. A. Swanke, Y. Cong, Z. Yao, H. Zeng, P. Fu, and A. Schnabel, IEEE J. Emerg. Sel. Top. Power Electron. **13**, 394 (2025).
[5] Y. Xiao, X. Lyu, J. Zhang, A. Yu, Y. Zheng, and R. Wang, Electronics. **15**, 1163 (2026).
[6] A. J. Grobler, S. R. Holm, and G. V. Schoor, IEEE Trans. Ind. Electron. **62**, 6756 (2015).
[7] C. Li, F.-C. Huang, Y.-Q. Wang, Proceedings of the Institution of Mechanical Engineers, Part I: Journal of Systems and Control Engineering. **231**, 43 (2017).
[8] T.-W. Lee, D.-K. Hong, Electronics. **12**, 2937 (2023).
[9] F. Xu, Doctoral dissertation, Investigation of High-Speed Permanent Magnet Motors with Toroidal Windings, University of Sheffield (2022).
[10] D. Lee, T. Balachandran, S. Sirimanna, N. Salk, A. Yoon, P. Xiao, J. Macks, Y. Yu, S. Lin, J. Schuh, P. Powell, and K. S. Haran, IEEE Trans. Ind. Appl. **59**, 1719 (2022).
[11] J. Zhao, W. He, W. Fu, Y. Ding, and Y. Guo, IEEE Access. **12**, 13431 (2024).
[12] H. Hong, J.-K. Lee, D.-H. Jung, J. Lee and H. Kim, IEEE Tran. Magn. **61**, 8201604 (2025).
[13] Z. A. Ren, K. Yu, Z. Lou, and C. Ye, IEEE Trans. Plasma Sci. **39**, 310 (2011).
[14] Z. A. Ren, K. X. Yu, Q. M. Xin, and Y. Pan, IEEE Trans.

Ind. Electron. **60**, 4891 (2013).
[15] Q. M. Xin, K. X. Yu, Q. L. You, and M. Yuan, IEEJ Trans. Elect. Electron. Eng. **10**, 44 (2015).
[16] L. J. Liu, K. X. Yu, and X. F. Xie, IEEE Trans. Plasma Sci. **47**, 2293 (2019).
[17] K. X. Yu, L. J. Liu, and X. F. Xie, IEEE Trans. Plasma Sci. **46**, 2949 (2018).
[18] J. T. Yang, C. Y. Ye, X. Liang, and F. Xiong, IEEE Trans. Plasma Sci. **47**, 2376 (2019).
[19] P. Tsao, M. Senesky, and S. R. Sanders, IEEE Trans. Ind. Appl. **39**, 1710 (2003).
[20] Z. Q. Liu, K. Wang, and F. Li, IEEE Trans. Magn. **55**, 8105706 (2019).
[21] Q. Li, J. T. Yang, S. D. Huang, P. Liu, Y. J. Feng, and L. Wang, IEEE Trans. Transp. Electrif. **8**, 1168 (2022).
[22] J. T. Yang, Q. Li, S. D. Huang, C. Y. Ye, P. Liu, B. Ma, and L. Wang, IEEE Trans. Ind. Electron. **69**, 7744 (2022).
[23] C. Ye, J. Yang, W. Xu, F. Xiong, and X. Liang, IEEE Trans. Magn. **54**, 1 (2018).
[24] J. T. Yang, C. Y. Ye, and S. D. Huang, IEEE Trans. Ind. Electron. **68**, 6504 (2021).
[25] K. Sivasubramaniam, T. Zhang, M. Lokhandwalla, E. T. Laskaris, J. W. Bray, B. Gerstler, M. R. Shah, and J. P. Alexander, IEEE Trans. Appl. Supercon. **19**, 1656 (2009).
[26] S. H. Lee, J. P. Hong, Y. K. Kwon, Y. S. Jo, and S. K. Baik, IEEE Trans. Appl. Supercond. **18**, 717 (2008).
[27] L. J. Liu, K. X. Yu, and X. F. Xie, 2023 IEEE International Conference on Power Science and Technology (ICPST), Kunming, China (2023) pp. 1-6.
[28] C. Ye, J. Yang, F. Xiong, and Z. Q. Zhu, IEEE Trans. Ind. Electron. **67**, 919 (2020).
[29] J. Yang, C. Ye, X. Liang, W. Xu, F. Xiong, Y. Xiang, and Li, W, IEEE Trans. Appl. Supercond. **28**, 1 (2018).
[30] F. D. Wei, J. H. Wang, and P. P. Liu, Electric Machines & Control Application **48**, 60 (2020).
[31] Z. Lou, Y. Cheng, Y. He, Q. Shen, X. Xie, and K. Yu, IEEE Trans. Plasma Sci. **43**, 1462 (2015).
[32] K. X. Yu, L. D. Jiang, S. L. Guo, X. Chen, and X. F. Xie, IEEE Trans. Plasma Sci. **51**, 544 (2023).
[33] P. Mellor, R. Wrobel, and N. Simpson, IEEE Energy Conversion Congress & Exposition (ECCE 2014), Pittsburgh, USA, pp. 5563-5570.
[34] Y. Amara, P. Reghem, and G. Barakat, IEEE Trans. Magn. **46**, 3481 (2010).
[35] M. Popescu and D. G. Dorrell, IEEE Trans. Magn. **49**, 3913 (2013).
[36] J. Pyrhnen, T. Jokinen, V. Hrabovcov, and H. Niemel, Design of Rotating Electrical Machines, Wiley, Chichester (2008) pp. 255-280.
[37] J. E. Vrancik, NASA, Cleveland, OH, Tech. Rep. D-4849, USA (1968).
[38] J. Wang, C. Guo, W. Zhou, and Q. Wan, Electronics. **13**, 2830 (2024).
[39] S. Wang, W. Yang, A. Tian, D. Song, and M. Bai, 2021 IEEE Sustainable Power and Energy Conference (iSPEC), Nanjing, China, pp. 3598-3604.
[40] L. J. Liu, K. X. Yu, X. F. Xie, G. X. Yan, and Z. J. Liu, IEEE Trans. Plasma Sci. **54**, 580 (2026).

Appendix [27]

The magneto potential of a PM is:

$$F_{pm} = \frac{l_m B_m}{\mu_0 \mu_r} \tag{A1}$$

Where, μ_0 and μ_r are the vacuum permeability and the relative permeability of the PM respectively, l_m and B_m are length and remanence of PM respectively. The magnetic resistance of a PM is:

$$R_m = \frac{l_m}{\mu_0 \mu_r A_{shell}} \tag{A2}$$

Where A_{shell} represents the cross-sectional area of the PM, which is calculated as:

$$A_{shell} = \frac{\pi}{4}(D^2{}_{shell} - D^2{}_o) \tag{A3}$$

Here, D_{shell} and D_o are the outer diameter of shell and stator core respectively. The magnetic reluctance of the leakage circuit is:

$$R_{ms} = \frac{l_m}{\mu_0 A_{ms}} \tag{A4}$$

Among them, A_{ms} represents the cross-sectional area of the magnetic leakage circuit, which is calculated as:

$$A_{ms} = \frac{\pi}{4}(D^2{}_o - D^2{}_{shaft}) \tag{A5}$$

Here, D_{shaft} is the diameter of rotor shaft. The main air-gap magnetic resistance is:

$$R_\delta = \frac{\delta}{\mu_0 A_\delta} \tag{A6}$$

Where A_δ represents the cross-sectional area of the main magnetic circuit, which is calculated as:

$$A_\delta = \pi D l \lambda^*{}_0 \tag{A7}$$

Where $\lambda^*{}_0$ represents the per-unit values of the DC component of air-gap permeance.